ISPRS Journal of Photogrammetry and Remote Sensing 224 (2025) 329–347

Contents lists available at ScienceDirect

ISPRS Journal of Photogrammetry and Remote Sensing

journal homepage: www.elsevier.com/locate/isprsjprs

On the consistency and stability of vegetation biophysical variables retrievals from Landsat-8/9 and Sentinel-2

Najib Djamai [a,*], Richard Fernandes [a], Lixin Sun [a], Gang Hong [a], Luke A. Brown [b], Harry Morris [c], Jadu Dash [d]

[a] Canada Centre for Remote Sensing, Natural Resources Canada, Ottawa, ON K1A 0E4, Canada
[b] School of Science, Engineering and Environment, University of Salford, Manchester, United Kingdom
[c] Climate and Earth Observation Group, National Physical Laboratory, Teddington, United Kingdom
[d] School of Geography and Environmental Science, University of Southampton, Southampton, United Kingdom

ARTICLE INFO

Keywords:
Validation
Landsat
Sentinel-2
LAI
fAPAR
Canopy cover

ABSTRACT

Systematic decametric resolution global mapping of vegetation biophysical variables, including fraction of absorbed photosynthetically active radiation (fAPAR), fraction of vegetation cover (fCOVER), and leaf area index (LAI), is required to support various activities, including climate adaptation, crop management, biodiversity monitoring, and ecosystem assessments. The Canada Centre for Remote Sensing (CCRS) version of the Simplified Level 2 Prototype Processor (SL2P-CCRS) enables global mapping of these variables using freely available medium resolution multispectral satellite data from Sentinel-2 (S2) and Landsat-8/9 (LS) data. In this study, fiducial reference measurements (RMs) from the National Ecological Observatory Network (NEON) supplemented with regional measurements from CCRS were used to evaluate the consistency between SL2P-CCRS estimates of fAPAR, fCOVER and LAI from LS and S2 data and to quantify their temporal stability. SL2P-CCRS estimates of fCOVER (Accuracy (A) ~ 0.03, Uncertainty (U) ~ 0.13) and fAPAR (A ~ −0.03, U ~ 0.13) from LS and S2 were unbiased, and generally similar between sensors, based on 6569 LS-RMs and 4932 S2-RMs matchups. However, LAI estimates, especially for woody wetlands, deciduous forest, and mixed forest, were underestimated, with better estimates obtained using S2 (A ~ −0.33, U ~ 0.98) than LS (A ~ −0.43, U ~ 1.13). For all variables, SL2P-CCRS LS estimates were highly correlated to S2 estimates overall (R2 0.80 to 0.82) but up to 35 % lower for LAI over broadleaf and mixed forests and between lower 10 % and 20 % otherwise. The inter-annual stability of SL2P-CCRS estimates from both LS and S2 fell within the Global Climate Observing System (GCOS) requirements with the mean (standard deviation) values of −0.01 yr^{-1} (0.06 yr^{-1}) for LS LAI, 0.02 yr^{-1} (0.09 yr^{-1}) for S2 LAI, and 0 yr^{-1} (0.01 yr^{-1}) for fCOVER and fAPAR from both LS and S2. The stability of both S2 and LS vegetation biophysical products indicate that are well suited for quantify the physical response of vegetation to climate variability, disturbances and regeneration.

1. Introduction

Systematic global mapping of vegetation biophysical variables, including fraction of absorbed photosynthetically active radiation (fAPAR), fraction of vegetation cover (fCOVER), and leaf area index (LAI), is required at decametric resolution to support climate adaptation, crop management, biodiversity monitoring, and ecosystem assessments (see Table 1; WMO, 2022; Group on Earth Observation Global Agricultural Monitoring, 2023; Group on Earth Observation Biodiversity Observation Network, 2023). Satellite data records (SDRs) of multispectral imagery are primary inputs for algorithms capable of mapping these variables globally (WGClimate, 2017). Currently, only the Sentinel-2A and Sentinel-2B (S2) and Landsat 8 and Landsat 9 (LS) imagers offer systematic global coverage of such SDRs at decametric resolution in a free and open manner (European Space Agency, 2013; Gascon et al., 2017; United States Geological Survey, 2019; United States Geological Survey, 2022).

Biophysical variables maps derived from LS and S2 imagery have attained Committee on Earth Observation Satellites (CEOS) Validation Stage 3 (NASA Land Product Validation Subgroup, 2024) based on

* Corresponding author.
E-mail address: najib.djamai@usherbrooke.ca (N. Djamai).

https://doi.org/10.1016/j.isprsjprs.2025.04.006
Received 26 August 2024; Received in revised form 2 February 2025; Accepted 2 April 2025
Available online 17 April 2025

Table 1
Vegetation biophysical variables definitions and Global Climate Observing System (GCOS) threshold thematic user requirements. Uncertainty corresponds to maximum of the absolute difference between the estimate and reference value as a percentage of the reference measurement and the absolute difference between the estimate and measurement value. Stability corresponds to the change in bias per year assuming fAPAR ∊ [0,1] and LAI ∊[0,10].

Acronym	Variable	Definition	GCOS requirements	
			Uncertainty	Stability
fAPAR	Fraction of absorbed photosynthetically active Radiation	Fraction of PAR effectively absorbed by plants (for direct sun illumination)	maximum (10 %, 0.05)	0.03 $year^{-1}$
fCOVER	Fraction of green vegetation cover	Green vegetation cover per unit horizontal ground area	maximum (10 %, 0.05	N/A
LAI	Leaf area index	Half the total green foliage area per unit horizontal ground area	maximum (20 %, 0.5)	0.06 $year^{-1}$

comparisons to fiducial reference measurements (RMs) at significant number of locations and time periods representative of global conditions (Fang et al., 2019; Ganguly et al., 2012; Kang et al., 2021; Brown et al., 2021a; Fernandes et al., 2023; Fernandes et al., 2024a; Amin et al., 2021). CEOS Stage 4 validation requires: i. quantification of the temporal stability of product accuracy, defined as the change in long-term bias at interannual time scales (Fernandes et al., 2014), to derive long-term trends and anomalies; and ii. the consistency between S2 and LS based products to satisfy the ≤10-day temporal resolution requirement of Global Climate Observing System (GCOS). CEOS Stage 4 validation of S2 and LS fAPAR, fCOVER and LAI products has not yet been achieved due to the limited temporal overlap of SDRs and RMs. Recently available multi-annual RMs representative of North American biomes, coincident with S2 and LS SDRs, opened possibilities for Stage 4 validation of vegetation products over North America (Brown et al., 2020a; Fernandes et al., 2024b).

Several globally applicable algorithms are available for mapping biophysical variables from LS and S2 bi-directional surface reflectance (reflectance, ρ) SDRs (Ganguly et al., 2012; Weiss and Baret, 2016; Pipia et al., 2021; Fernandes et al., 2024a; Wan et al., 2024). These algorithms use either look-up-table or regression estimators, both calibrated using either canopy radiative transfer models (RTMs), other products, or empirical databases (Baret and Buis, 2008; Fang et al., 2019; Ma and Liang, 2022). In this study, we consider algorithms calibrated using RTMs since the same code and priors can be applied to both S2 and LS SDRs with minor changes in sensor specifications (Weiss and Baret, 2020), and since they are widely used for mapping coarse resolution vegetation variables products (Lacaze et al., 2015; Yan et al., 2016; Disney et al., 2016; Yan et al., 2018; Fang et al., 2019).

RTMs represent vegetation using either spatially homogeneous or spatially heterogenous patterns (Widlowski et al., 2007). Numerical and empirical studies indicate that heterogeneous RTMs are required for unbiased LAI estimation over shrubs and forests (Myneni et al., 1997; Shabanov et al., 2005; Gonsamo and Chen, 2014; Brown et al., 2019; Fernandes et al., 2024a). The Landsat equivalent of the MODIS fAPAR/LAI algorithm (Ganguly et al., 2012) and the Canada Centre for Remote Sensing (CCRS) version of the S2 Simplified Level 2 Prototype Processor (S2LP-CCRS, Fernandes et al., 2024a) use heterogeneous RTMs. This study validates SL2P-CCRS since its free and open code allows it to be recalibrated and applied to both LS and S2. For a given sensor, SL2P-CCRS uses four land cover specific neural network regression algorithms for needleleaf forest (NF), broadleaf forest (BF), mixed forest (MF) and other land cover classes (OTHER) to estimate a given biophysical variable. Each algorithm being calibrated using radiative transfer model simulations with parameters for land surface conditions, acquisition geometry and spectral characteristics sampled from priors representative of global Sentinel-2 or Landsat Operation Line Imager acquisitions.

For this study, SL2P-CCRS regressions were recalibrated for LS using a calibration database produced by applying LS spectral response functions (NASA Landsat Science, 2013) to a database of 1 nm resolution ρ simulated using the sampling scheme, same RTM and priors as used for S2 but with uniform sampling of LS acquisition geometry. Identical priors and RTMs were used to increase the consistency between LS and S2 estimates, to the extent the algorithms are not overly sensitive to differences in spectral sampling, acquisition geometry, and spatial resolution. Nevertheless, studies using regression algorithms calibrated with SAILH model suggest LS retrievals could have greater uncertainty than coincident S2 retrievals for canopies with high LAI values due to the absence of equivalent S2 red-edge bands with LS data (Djamai and Fernandes, 2018; Dong et al., 2023). User requirements for products based on these algorithms are cited in terms of uncertainty and stability for retrievals at a given location (World Meteorological Organization (WMO), 2022); with uncertainty defined in a general sense as " a parameter, associated with the result of a measurement, that characterizes the dispersion of the values that could reasonably be attributed to the measurand" (Working Group 1 of the Joint Committee for Guides in Metrology, 2008) and stability defined in the long-term change in bias over time where bias corresponds to the expected value of the difference between the measurement and reference (Fernandes et al., 2014). As such, it is essential to quantify the relative uncertainty and bias between S2 and LS vegetation variables estimates to facilitate characterization of seasonal vegetation dynamics and long-term vegetation trends.

CEOS recommends using both comparison to RMs (validation) and comparison of products (intercomparison) to quantify the thematic performance of different combinations of mapping algorithms and SDRs (Fernandes et al., 2014). Validation allows one to quantify whether the likelihood products would satisfy user requirements and to identify systematic limitations due to SDRs or algorithms. In this study, SL2P-CCRS S2 and LS retrievals are validated over the same sites, although with different temporal sampling, to address both tasks. Intercomparison is also conducted over the validation sites to determine if the validation results are also reflected in between-product differences. CEOS has not previously identified methods for quantifying the temporal stability of vegetation variables estimates from products. Thus, statistics corresponding to both the expected value and confidence interval of stability are derived for fAPAR, fCOVER and LAI products here for the first time.

Our study addressed two questions based on the performed validation and intercomparison:

1. How do SL2P-CCRS fAPAR, fCOVER, and LAI estimates from LS compare to estimates from S2 in terms of accuracy (A), precision (P) and uncertainty (U) with respect to RMs and in terms of product intercomparison?
2. What is the stability (S) of products estimates from LS and S2 over North American sites with sufficient RMs temporal samples?

We hypothesized that:

1. LS fAPAR and fCOVER will be similar to corresponding S2 estimates and have similar A, P, U but LS LAI will show a larger negative bias and greater uncertainty compared to S2 due to LS having no red-edge bands.

2. Both LS and S2 will show much lower S (i.e. better) than retrieval uncertainty since stability is less sensitive to local biases due to RTM error or uncertainties in specification of priors required for RTM inversion.

The study scope was limited to vegetated North American sites, where multi-annual sampling of RMs were available for numerous sites. The scope was further limited in that S2 SDRs only spanned 2019 to 2023 due to the absence of recently processed S2 Collection 1 SDRs on the Google Earth Engine (GEE) platform on which SL2P-CCRS is currently deployed. Even so, our study included the largest validation dataset applied to simultaneously validate LS and S2 fAPAR, fCOVER and LAI over North America to date.

Our study is novel in that, i. it is the first study to provide a Stage 4 validation of a globally applicable system for mapping both vegetation variables from S2 and LS SDRs, ii. it presents a first quantification of stability of derived products, and iii. it quantifies the consistency of S2 and LS based products using a representative sample of matchups. We expect that users will gain a better understanding of the thematic performance of both LS and S2 products from SL2P-CCRS, especially with respect to time series stability over regions representative of our validation sites. Our findings will also provide algorithm producers a better understanding of conditions under which improvements are needed to satisfy user requirements, as well as a characterization of a baseline mapping system (SL2P-CCRS) for benchmarking new algorithms. Finally, the methods presented will contribute to improve good practice for product validation.

2. Materials and methods

2.1. Materials

2.1.1. Reference measurements

RMs were acquired at 47 National Ecological Observatory Network (NEON, 2024) and 10 CCRS sites across North America (Fig. 1; Table A1 in Appendix A). These 57 sites corresponding to 47 sites used for

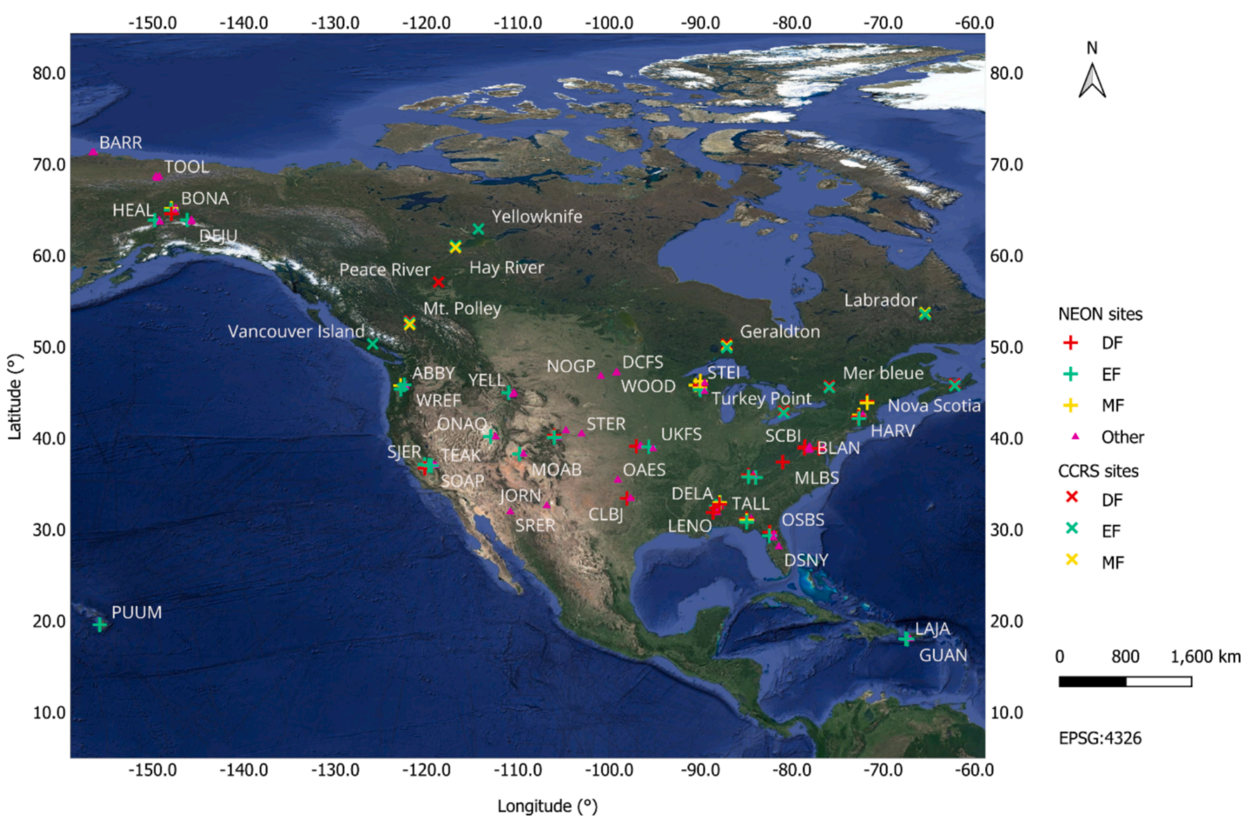

Fig. 1. NEON and CCRS sites across North America. Symbols indicate dominant NLCD forest class or otherwise.

Table 2
NEON and CCRS Elementary Sampling Units (ESUs) and reference measurements (RMs) by National Land Cover Database (NLCD) class (forested classes are in bold). SL2P-CCRS algorithm is indicated for each class.

NLCD land cover class (Abbrev.)	SL2P-CCRS Groupings of NLCD classes	NEON		CCRS	
		#ESUs	#RM	#ESUs	#RMs
Evergreen forest (EF)	NF	263	3427	9	48
Deciduous forest (DF)	BF	249	3923	5	7
Mixed forest (MF)	MF	49	639	3	9
Woody wetland (WW)	BF	88	326	0	0
Cultivated crops (CC)	OTHER	50	702	0	0
Emergent herbaceous wetland (EHW)	OTHER	19	79	0	0
Grassland herbaceous (GH)	OTHER	165	2101	0	0
Pasture hay (PH)	OTHER	32	934	0	0
Sedge herbaceous (SH)	OTHER	20	126	0	0
Shrub scrub (SS)	OTHER	139	1704	0	0
Total		1074	13,961	17	64

previous S2 validation studies (Brown et al., 2021b; Fernandes et al., 2023; Fernandes et al., 2024a) and 10 additional NEON sites. NEON sites are representative of 20 North American ecoclimatic domains and span 11 United States of America National Land Cover Database classes (NLCD) (USGS, 2024) (Table 2). A total of 1074 20 m × 20 m square elementary sampling units (ESUs) were visited across the NEON sites during the growing seasons of 2013 through 2022. For each NEON site, a minimum of three ESUs were sampled bi-weekly during the growing season at each NEON site and the remainder were sampled near peak season.

Additionally, 48 EF, 7 DF, and 9 MF ESUs were measured across the CCRS sites; with each 30 m × 35 m ESU sampled once during July and August between 2019 and 2020. For both NEON and CCRS, fAPAR, fCOVER, and LAI RMs were simultaneously measured at each ESU on each sampling date.) and 10 CCRS sites across North America (Fig. 1; Table A1 in Appendix A). These 57 sites corresponding to 47 sites used for previous S2 validation studies (Brown et al., 2021b; Fernandes et al., 2023; Fernandes et al., 2024a) and 10 additional NEON sites. NEON sites are representative of 20 North American ecoclimatic domains and span 11 United States of America NLCD classes (Table 2). A total of 1074 elementary sampling units (ESUs) were visited across the NEON sites during the growing seasons of 2013 through 2022. For each NEON site, a minimum of three ESUs were sampled bi-weekly during the growing season at each NEON site and the remainder were sampled near peak season. Additionally, 48 EF, 7 DF, and 9 MF ESUs were measured across the CCRS sites; with each ESU sampled once during July and August between 2019 and 2020. For both NEON and CCRS, fAPAR, fCOVER, and LAI RMs were simultaneously measured at each ESU on each sampling date.

RMs were derived from in-situ digital hemispherical photographs (DHPs), processed using free and open-access software packages, corrected for biases due to woody material using empirical or site-specific calibration, and characterized in terms of uncertainty using RMs for vegetation protocols. These approaches are documented in previous studies (Brown et al., 2021a; Fernandes et al., 2023; Fernandes et al., 2024a), so only details relevant to the current study are given below.

DHPs were measured within a 20 m square for the NEON sites and 15 m × 35 m rectangle for the CCRS sites, centred on each ESU using a cross-sampling design for the NEON sites and two parallel 35 m long transects for the CCRS sites. For each date, co-located upward and downward looking DHPs were sampled at ~1 m height at 12 locations for the NEON sites and 14 locations for the CCRS sites, spaced evenly along the sampled cross or line transects. NEON DHPs were acquired using 36.3-megapixel Nikon D810 or D800 cameras (Nikon, 2024a) with a Nikon 16 mm Fisheye lens (Nikon, 2024b). CCRS DHPs were acquired using 45.7-megapixel Nikon D850 cameras (Nikon, 2024c) with a Nikon 8 mm Fisheye lens (Nikon, 2024d). Both NEON and CCRS DHPs corresponded a 180° diagonal field of view. As in Brown et al. (2020a), DHP images were visually quality controlled ESUs with images demonstrating fixed pattern noise, overexposure, colour balance issues, variable illumination, or foreign objects within the field-of-view were discarded, as were ESUs with less than 12 images or images acquired in lossy formats. For CCRS, enhanced using Nikon ViewNX-I (Nikon, 2024e) to improve visual separation of canopy versus soil or sky. Only regions in images within 60° of nadir were processed to constrain the spatial footprint of measurements and minimize RM uncertainty due to camera tilt. Subsequently, the spatial support of downward measurements fell within the nominal ESU boundary while the spatial support of upward measurements was a circle centred on the ESU with diameter ~1.5 times the canopy height (Fernandes et al. 2023).

HemiPy (Brown et al., 2023) and CAN-EYE V6.45 (INRAE, 2022) were respectively used to estimate the fraction of woody and green cover per horizontal ground area (fCANOPY), the fraction of PAR intercepted by woody and green elements (fIPAR), and plant area index (PAI) defined as half of the total vegetation surface area per unit horizontal ground area at the NEON and CCRS sites. PAI was corrected for clumping using the approach of Lang and Yueqin (1986) corresponding to an expected bias of ~−5 % and upper bound on bias of ~−10 % (Fernandes et al., 2024a). RMs uncertainty was quantified as described in Fernandes et al. (2023) and Brown et al. (2021b).

Coefficients corresponding to the woody-to-total area ratio were applied to relate fCANOPY, fIPAR, and PAI to fCOVER, fAPAR, and LAI (Table B1 in Appendix B). For canopies with a height less than 19 m, coefficients were estimated from values based on destructive sampling at sites with the same land cover class (Brown et al., 2021a). ESU specific coefficients were derived for NEON overstory canopies with >=19 m tall using CAN-EYE as qualitative assessment of DHPs showed far greater woody area than expected based on woody-to-total area ratios for shorter canopies with the same land cover. For these NEON ESUs, CANEYE was first applied to DHP imagery to estimate PAI and then applied once more to the DHP imagery, enhanced using View-NXi to highlight green pixels, to estimate LAI (Appendix C, Table C1). This approach required manual labelling of substantial portions of imagery, so it was not feasible to apply for LAI estimation for all sites. This approach has not been validated for NEON ESUs so an uncertainty of 0.19 for the ratio of woody-to-total area is assumed based on validation of a similar approach using HemiPy over a broadleaf forest (Brown et al. 2021b). ESU fAPAR, fCOVER, and LAI RM estimates and their uncertainties were derived by a weighted sum of corresponding overstory, and understory measurements described in Brown et al. (2021a).

2.1.2. Satellite data

GEE LS Level 2 (L2) LANDSAT/LC08/C02/T1_L2 (Google Earth Engine, 2013), LANDSAT/LC09/C02/T1_L2 Google Earth Engine, 2021) and S2 Level-2A (L2A) (Google Earth Engine, 2017) ρ products were used as input to SL2P-CCRS. These data are reformatted versions of original USGS products (for LS) and European Space Agency (for S2) Level 2 ρ products.

LS L2 products include ρ gridded at 15 m resolution for one panchromatic band and 30 m resolution for nine bands within the shortwave spectrum (Table 3) derived from Operational Land Imager (Knight and Kvaran, 2014; Levy et al., 2024) measurements of top-of-atmosphere radiance using the Landsat Surface Reflectance Code (Vermote et al., 2018), in addition to the acquisition geometry, and a mask indicating clear sky land pixels based on the fMASK4.0 algorithm (Qiu et al., 2019). LS L2 products have a geolocation uncertainty of <13 m 90 % circular error probable (CEP; Storey et al., 2014) and a radiometric uncertainty of ~0.05ρ + 0.005 for flat terrain (Doxani et al., 2018). fMASK 4.0 has a clear sky omission error of 4.8 % and commission error of 4.6 % (Qiu et al., 2019).

S2 L2A products include ρ gridded at 10 m resolution for four bands, 20 m resolution for six bands and 60 m resolution for three bands derived from Multispectral Instrument (Drusch et al., 2012) measurements of top-of-atmosphere radiance using Sen2Cor Version 2.4.0 (Müller-Wilm, 2018, Table 4), as well as the mean acquisition geometry for the product granule and a gridded 20 m resolution scene classification map indicating clear sky land pixels. S2 L2A products have a geolocation uncertainty < 12.5 m 95 % CEP (Gascon et al., 2017) and a radiometric uncertainty of ~0.05ρ + 0.005 for flat terrain (Djamai and

Table 3
LS bands (SL2P-CCRS input bands are in bold).

Band	Resolution (m)	Central Wavelength (nm)	Description
B1	30	443	Coastal/Aerosol
B2	30	482	Blue
B3	**30**	**562**	**Green**
B4	**30**	**655**	**Red**
B5	**30**	**865**	**Near-Infrared**
B6	**30**	**1610**	**Short Wave Infrared**
B7	**30**	**2200**	**Short Wave Infrared**
B8	15	590	Panchromatic
B9	30	1375	Cirrus

Table 4
S2 bands (SL2P-CCRS input bands are in bold).

Band	Resolution (m)	Central Wavelength (nm)	Description
B1	60	443	Coastal/Aerosol
B2	10	490	Blue
B3	**10**	**560**	**Green**
B4	**10**	**665**	**Red**
B5	**20**	**705**	**Vegetation red edge**
B6	**20**	**740**	**Vegetation red edge**
B7	**20**	**783**	**Vegetation red edge**
B8	10	842	Near-Infrared
B8a	**20**	**865**	**Near-Infrared**
B9	60	940	Water vapour
B10	60	1375	Cirrus
B11	**20**	**1610**	**Short Wave Infrared**
B12	**20**	**2190**	**Short Wave Infrared (SWIR)**

Fernandes, 2018; Doxani et al., 2018). Sen2Cor has a clear sky omission error of 3 % and commission error of 6 % (European Space Agency, 2020). For each L2A product, the matching S2Cloudless cloud probability product (Zupanc, 2017) was used to reduce clear sky commission errors. L2A product pixels were flagged as cloudy if the S2Cloudless cloud probability was greater than 50 %.

2.1.3. Land cover

The 30 m resolution circa 2020 North America Land Cover Monitoring System (NALCMS) land cover map was used to determine the SL2P-CCRS regression algorithm applied to each S2 or LS pixel (Table 2). The thematic error of NALCMS product has been assessed over Canada with 79.9 % correct labelling for all 18 classes and 83 % correct labelling of forest classes (Latifovic et al., 2012). NALCMS products matched the nominal LS sampling grid, so resampling was not required when using SL2P-CCRS with LS SDRs. Nearest neighbour resampling was used to assign NALCMS land cover to 20 m S2 pixels. Additional uncertainty in SL2P-CCRS S2 retrievals due to resampling was negligible as ESUs were located within patches of undisturbed homogeneous land covers (Brown et al., 2020a; Fernandes et al., 2023) and the SL2P-CCRS RTM land cover classes were highly generalized.

2.2. Methods

2.2.1. NEON RMs quality control

NEON RMs were subjected to additional quality control since HemiPy, in contrast to CANEYE, is completely automated. This resulted in rare cases where images with poor exposure or illumination resulted in excess shadows that were classified in vegetation. Since such cases were isolated in time, we used a time series filter to detect and censor them. For each variable, a moving window temporal filtering was applied to measurements at each ESU to identify spurious RMs. The i^{th} RM (RM_i) with associated uncertainty $\widetilde{RM}_i$, was flagged as spurious if the three following conditions held simultaneously:

$$|RM_i - RM_l| > \max\left(\widetilde{RM}_i, \varepsilon_V\right) \quad (1)$$

$$|RM_i - RM_r| > \max\left(\widetilde{RM}_i, \varepsilon_V\right) \quad (2)$$

$$(RM_i - RM_l).(RM_i - RM_r) > 0 \quad (3)$$

where RM_l and RM_r are respectively the previous and the next RMs acquired within $+/-15$ days and ε_V is an empirical land cover specific threshold (e.g. Fig. C1 in Appendix C). Eqs. (1) and (2) identified measurements whose first derivative exceed the actual magnitude of the estimate, and the maximum expected absolute uncertainty of non-outlier estimates while Eq. (3) only censored identified measurements for time periods with monotonic trends to preserve peak or minimum phenology values. Only 0.31 % of LAI, 0.97 % of fCOVER, and 0.93 % of fAPAR RMs were flagged and removed from validation (Table C1 in Appendix C).

2.2.2. Correcting NEON RMs estimates for ESUs with moss

Exploratory data analysis identified a constant SL2P-CCRS bias of ~0.9 for LAI, ~0.25 for fAPAR, and ~0.25 for fCOVER for RMs from Alaskan tundra sedge sites (BARR, TOOL, and DEJU) for both LS and S2 (Fig. C1 in Appendix C). These sites had only downward DHPs as overstory vegetation was absent. Examination of DHPs indicated virtually 100 % moss cover that had been labelled by HemiPy as non-vegetated area. Moss canopy LAI values range from 1 to over 20, with significant between species differences (Niinemets and Tobias, 2019). Moss canopy LAI is inversely correlated with leaf thickness so the functional role of moss LAI in controlling carbon and water fluxes differs from vascular plants (Zotz and Kahler, 2007). For example, Niinemets and Tobias (2019) noted that "for acrocarpous moss *T. ruralis*, already the upper 2 mm of canopy reduces the light level to only 20 % of incident light". This suggests that moss LAI cannot be considered directly when validating satellite LAI products since the high LAI values are accompanied by extremely thin foliage with different functional and structural characteristics to vascular vegetation. At the same time, a method is required to characterize the ability of satellite products to track vascular LAI at mossy sites. Keeping in mind the limitation to vascular LAI, RMs for all mossy ESUs were increased by the observed bias between all satellite products and RMs matchups, irrespective of sensor. Land cover specific thematic metrics were reported to isolate this class should our approach be refined by future studies.

2.2.3. Estimation of LS and S2 vegetation variables

The Landscape Evolution and Forecasting (LEAF; Fernandes et al., 2021) was used to extract LS and S2 L2A clear sky land pixels whose centroid fell within 30 m of an ESU centroid, for S2, and 45 m, for LS, of an ESU centroid and within ±7 days of a RM. The nearest NALCMS land cover pixel was associated with each sampled S2 and LS reflectance.

A Python implementation of SL2P-CCRS (Djamai, 2024), identical to that implemented in the GEE code for LEAF, was applied to each sampled measurement. SL2P-CCRS uses separate land cover specific neural networks correspond to groupings of NLCD classes (Table 2), using ρ measured for a LS or S2 pixel (Table 3 for LS and Table 4 for S2) together with available acquisition geometry, to estimate each variable. All neural networks correspond to a single, 5 tangent-sigmoid node, hidden layer network identical to that used in the original SL2P algorithm (Weiss and Baret, 2016) and calibrated using batch training as described in Fernandes et al. 2023. Additionally, SL2P-CCRS flags measurement whose ρ does not lie within $+/-0.05$ of RTM simulations used for calibration or if the estimate falls outside the range of variable values within the simulations. NF and BF algorithms are calibrated using simulations produced by applying sensor specific spectral response functions to database of 1 nm resolution ρ simulated by the 4SAIL2 heterogeneous RTM (Verhoef and Bach 2007) sampled with representative priors calibrated with field measurements available prior to 2024 and nominal sensor acquisition geometry (Fernandes et al. 2024a). Previously, SL2P-CCRS used the average of the NF and BF algorithm estimates for MF. In this study, the MF algorithm is updated to use the same neural network architecture as the BF algorithm but a calibration database using 4SAIL2 simulations with input parameters sampled from the union of the BF and NF priors. The OTHER class is mapped using the SL2P algorithm (Weiss and Baret, 2016) based on the 4SAIL homogeneous RTM (Verhoef, 1985) with priors corresponding to global in-situ measurements available prior to 2016.

For each biophysical variable, the trimmed median residual between a given RM and matching SL2P-CCRS estimates was computed for S2 and LS products. Trimming corresponded to discarding residuals exceeding the 90 %ile for a given RM. It was applied since perfect spatial matching and clear sky identification was not possible for the large sample size used in our study, and it did not result in changes in statistical tests of differences in performance between sensors or estimates of stability but improved the representativeness of the measurement error modelled when fitting conditional A, P, U curves.

2.2.4. Validation and intercomparison

Following good practice (Fernandes et al., 2014) scatter plots as well as the population A, U, coefficient of determination (R^2), and uncertainty agreement ratio (UAR) were computed separately for LS and S2 products for all matchups and for each NLCD class based on the following equations.

$$A = \frac{1}{N}\sum_{i=1}^{N} (\hat{y}_i - y_i) \tag{4}$$

$$U = \sqrt[2]{\frac{1}{N}\sum_{i=1}^{N} (\hat{y}_i - y_i)^2} \tag{5}$$

$$P = \sqrt[2]{\frac{1}{N}\sum_{i=1}^{N} (\hat{y}_i - y_i - A)^2} \tag{6}$$

$$R^2 = \left[\frac{\sum_{i=1}^{N} (\hat{y}_i - \overline{\hat{y}}).(y_i - \overline{y}))}{\sum_{i=1}^{N} (\hat{y}_i - \overline{\hat{y}})^2.(y_i - \overline{y})^2}\right]^2 \tag{7}$$

$$UAR = \frac{1}{N}\sum_{i=1}^{N} I\left(\left|\frac{\hat{y}_i - y_i}{y_i}\right| \le \varepsilon_{rel} \cup |\hat{y}_i - y_i| \le \varepsilon_{max}\right) \tag{8}$$

where, $\hat{y}_i$, y_i are respectively the SL2P-CCRS estimate and RM for the $\underline{i^{th}}$ of N comparisons, $\overline{y}$, $\overline{\hat{y}}$ are their corresponding average values, ε_{rel}, ε_{max} are respectively the relative and maximum target uncertainty requirement, and I is the indicator function.

Good practice also requires quantifying the A, P and U conditional on a given RM value to reduce the impact of the sampling distribution of RMs on validation results and to isolate problematic retrieval conditions (Fernandes et al., 2014). Ideally, one would have sufficient samples to produce conditional A, P and U curves for each NLCD class. Due to the imbalanced nature of RMs sampling within a given NLCD class, conditional A, P, U curves were fitted for RMs grouped as either forested or non-forested ESUs. This partitioning was useful since SL2P-CCRS assumes a homogenous canopy for non-forested classes and a heterogeneous canopy for forested classes (Fernandes et al., 2024a). For each group and sensor, A and U, conditional on either the RM (producer validation) or the product estimates (user validation), were estimated by fitting third order polynomial weighted least squares regressions to residuals and absolute residuals as described in Fernandes et al. (2023). Weights corresponded to the Euclidean sum of the standard error of sampled product estimates and the RM one standard deviation. P, conditional on the RM, was estimated by fitting third order polynomial weighted least squares regressions to absolute residuals after first subtracting the modelled conditional A.

Intercomparison was performed using all clear sky S2 and LS ρ data between April and September inclusively for 3 × 3 pixels centred on each ESU whose dates matched within +/−1 day. SL2P-CCRS was applied to each sampled measurement to produce estimates of fAPAR, fCOVER, and LAI. Following good practice, kernel density plots of matchups for groupings of NLCD classes corresponding to SL2P-CCRS neural network regression algorithms, and, given the fact there were sufficient intercomparisons samples for each NLCD class, NLCD class specific A and U statistics were derived.

At each site, for each NLCD class present, S was estimated as the slope of the ordinary least squares regression of the average annual bias of ESUs corresponding to that NCLD class (see Fig. E1 in Appendix E). The 95 % confidence interval of the regression slope was used as the precision of estimated S. Only results for sites with at least 5 years for LS, or 4 years for S2, due to the shorter input records, with at least 5 interannual samples per year were reported. GCOS indicates that stability should be reported using units expressed as % change in bias per decade (GCOS, 2022). However, given that S was quantified with as few as 5 years at some sites we use units of % change in bias per year to avoid an implication that we actually used 10 years of annual bias estimates at all sites. This approach is still in compliance with CEOS good practices for validation (Fernandes et al., 2014) cited in the GCOS requirements (GCOS, 2022). Additionally, the 95 % confidence interval of the S quantify the potential decrease in precision of our estimates of S due to at sites with less than 10 years of comparisons.

3. Results

3.1. Validation

A total of 4932 S2-RM matchups (Fig. 2) and 6569 LS-RM (Fig. 3) matchups were used during validation. The RMs range of LAI, fCOVER, and fAPAR matchups are, respectively, [0.0, 6.87], [0, 0.99], and [0, 0.95] for S2, and [0.02, 5.88], [0, 0.96], and [0, 0. 93] for LS. RM histograms were qualitatively similar between sensors although LS had a slightly greater relative frequency of extreme values. However, RMs histograms differed between NLCD land cover, with forest classes dominating values above the 50 %ile for each variable. For fCOVER and fAPAR, S2 and LS R^2, A, U and UAR for all matchups were virtually identical at respectively ~0.8, ~0.03, ~0.13 and ~0.60. However, for LAI, A, U, and UAR were better for S2 (respectively, 0.33, 0.98, and 0.65) compared to LS (respectively, 0.43, 1.13, and 0.51).

The of matchups by land cover class were comparable between S2 and LS (Fig. 4) with the most matchups over the EF and DF forest classes primarily due to the considerable number of ESUs for these classes (Table 2). EHW and SH had the least matchups, ranging between 35 and 79 depending on sensor and NLCD class (Tables D1 and D2 in Appendix D). Between sensors, difference in metrics were, in most cases, smaller than the between land cover differences, with the largest between sensor A (U) difference of ~0.4 (~0.32) for LAI observed for DF, ~0.04 (~0.03) for fCOVER observed for MF and EHW, and ~0.03 (~0.02) for fAPAR observed for MF and GH. However, substantial differences in A and U were observed between forested and non-forested classes. In terms of accuracy, forested classes were underestimated by between ~0.5 and ~2 for LAI and between ~0.05 and ~0.20 for fAPAR, while non-forested classes were slightly overestimated by ~0.5 for LAI and ~0.1 for fAPAR (Fig. 4). fCOVER was also slightly overestimated for non-forest classes but was almost unbiased for forest classes. LAI U ranged between ~0.2 and ~0.7 for non-forested classes and between ~0.8 and ~2 for forested classes. However, fCOVER and fAPAR U, both ranging between ~0.05 and 0.20, did not show systematic forest/non-forest trends, indicating that the accuracy error contributes more to U for LAI than fAPAR and fCOVER.

Conditional A, P, U curves were generally monotonic for forested classes except for extreme fCOVER and fAPAR values where sampling was limited (Fig. 5). For LS, LAI A trended quasi-linearly from ~0.5 at LAI 0 to ~−3 at LAI 6, while both fCOVER and fAPAR A trended monotonically from ~0.15 at very low values to ~−0.15 at the highest values. LS P was almost constant across the range of each variable at

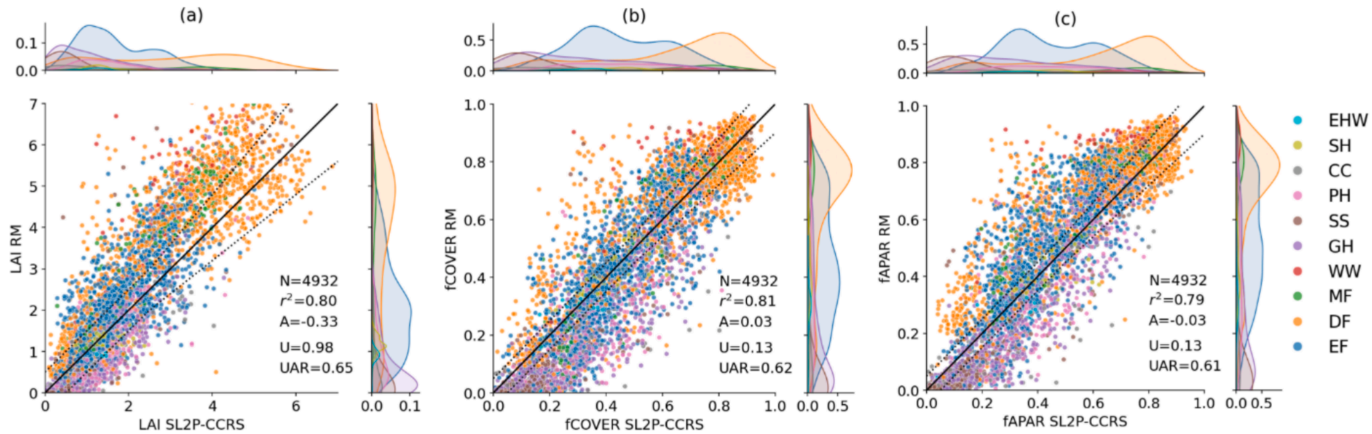

Fig. 2. Scatter plots of SL2P-CCRS estimates of LAI (a), fCOVER (b), and fAPAR (c) obtained from S2 data versus matching RMs together with population validation metrics. Dashed lines bound target user requirement around solid 1:1 line. Colours corresponds to NLCD land cover class.

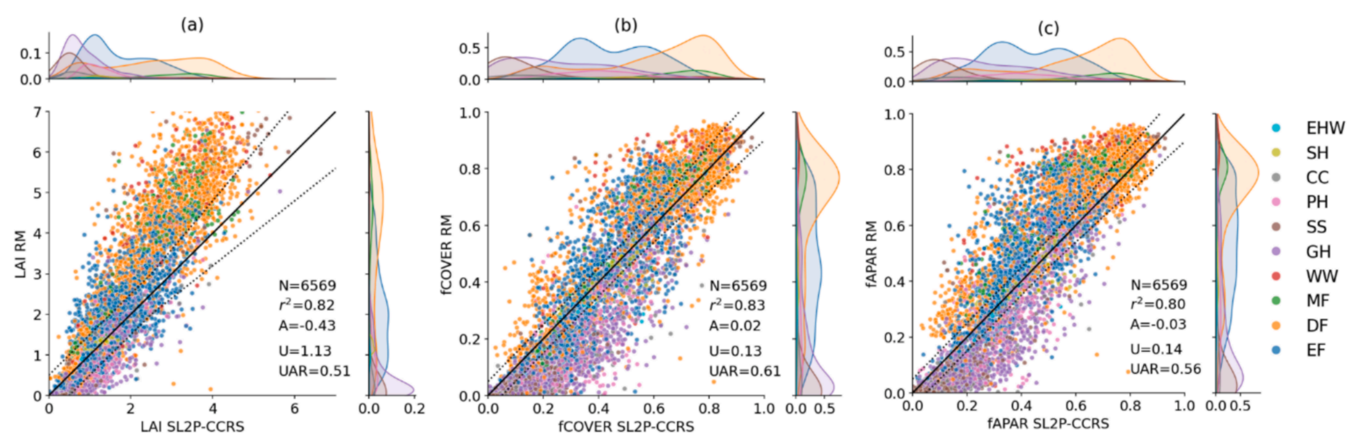

Fig. 3. Scatter plots of SL2P-CCRS estimates of LAI (a), fCOVER (b) and fAPAR (c) obtained from LS data versus matching RMs together with population validation metrics. Dashed lines bound target user requirement around solid 1:1 line. Colours corresponds to NLCD land cover class.

∼0.5 for LAI, ∼0.08 fCOVER, and ∼0.09 for fAPAR. As a result, LS LAI U increased from ∼0.1 at LAI 0 to ∼3 at LAI 7. LS fCOVER and fAPAR U was typically ∼0.1 but increased to ∼0.15 at extremely low values due to a positive bias. S2 LAI A was similar to LS for LAI < 3 but showed a proportional improvement over LS for LAI > 3, with an A of ∼−2 at LAI 7 versus ∼−3 for LS. The improvement in A for S2 versus LS combined with similar P for both sensors translated into a modest improvement in S2 U compared to LS for LAI > 3 but only minor differences for LAI < 3. fCOVER and fAPAR A were slightly better for S2 versus LS above fCOVER > 0.5 and fAPAR > 0.7, respectively, but otherwise no significant between-sensor differences were observed for these variables.

Conditional A, P, U curves for non-forested classes were quasi-monotonic for LAI, with only slight improvements for S2 versus LS at LAI > 4 and fCOVER or fAPAR > 0.7 (Fig. 6). For both S2 and LS, LAI A showed a similar trend as observed for forests, but with underestimation reaching ∼−2.5 rather than ∼−3 at LAI 7. Precision error was ∼0 at LAI 0 and gradually increased to ∼1 at LAI 5. As a result, LAI U increased gradually with LAI reaching ∼2.5 at LAI 7. P for fCOVER and fAPAR was almost constant at ∼0.8 and ∼0.6, respectively. However, sinusoidal A and U curves were observed for fCOVER with overestimation below 0.5 and underestimation for larger values. Additionally, a positive inflection in U was observed for fCOVER and fAPAR > 0.9 but this is likely due to insufficient samples to constrain the 3rd order polynomial fit.

3.2. Intercomparison

Intercomparison resulted in ∼11,800 NF, ∼13,200 BF, ∼2000 MF and ∼19,000 OTHER matchups for each variable (Fig. 7, Table E1 in Appendix E). For fCOVER and fAPAR, LS and S2 retrievals agreed within 0.15 at 50 %ile and 0.20 at 10 %ile irrespective of land cover, with S2 estimates slightly higher than matching LS estimates (linear regression slope of ∼0.88) although overall correlation was high (R2 0.80 to 0.83, Appendix E).

LAI intercomparisons, in contrast to fAPAR and fCOVER, were different between NF and OTHER classes versus BF and MF classes although overall correlation between LS and S2 was high (R2 0.80, Appendix E). For NF and OTHER, LAI agreed within 0.5 at 50 %ile and 1 at 10 %ile with a linear regression slope of 0.82 for NF and 0.80 for OTHER, indicating S2 LAI was slightly higher than matching LS LAI. In contrast, the linear regression slope of 0.62 for BF and 0.67 for MF indicated S2 LAI was consistently larger than LS LAI.

The same metrics shown in Fig. 4 were also computed for intercomparisons (Fig. 8) to determine the relative magnitude of between-sensor differences versus differences between each sensor and RMs for each NLCD class.

For LAI, intercomparison A was ∼0 for non-forested and EF classes and ranged from ∼−0.25 to ∼−0.55 for WW, MF, and DF classes. fAPAR and fCOVER intercomparison A were bimodal between non-forested and

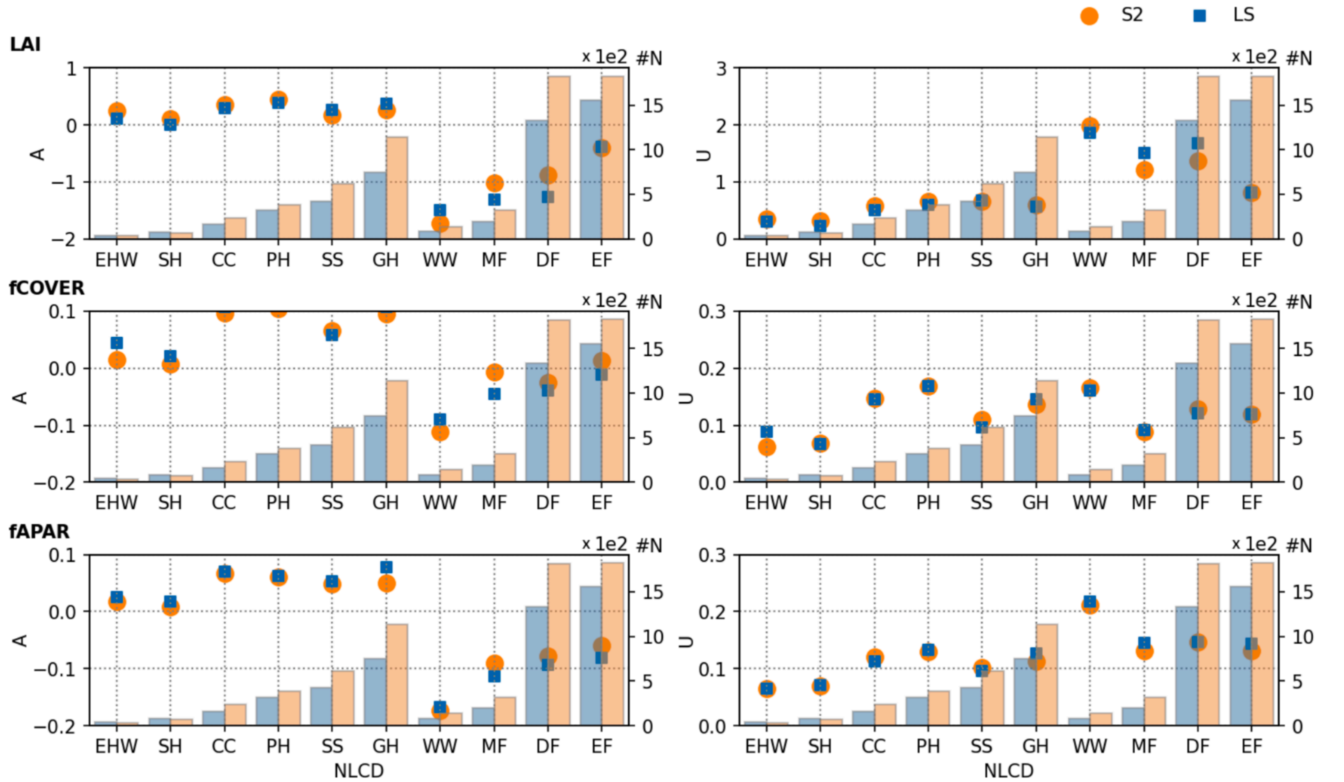

Fig. 4. NLCD class specific A and U validation statistics for SL2P-CCRS estimates of LAI, fCOVER, and fAPAR obtained from LS and S2 data together with match-up sample size N (histograms).

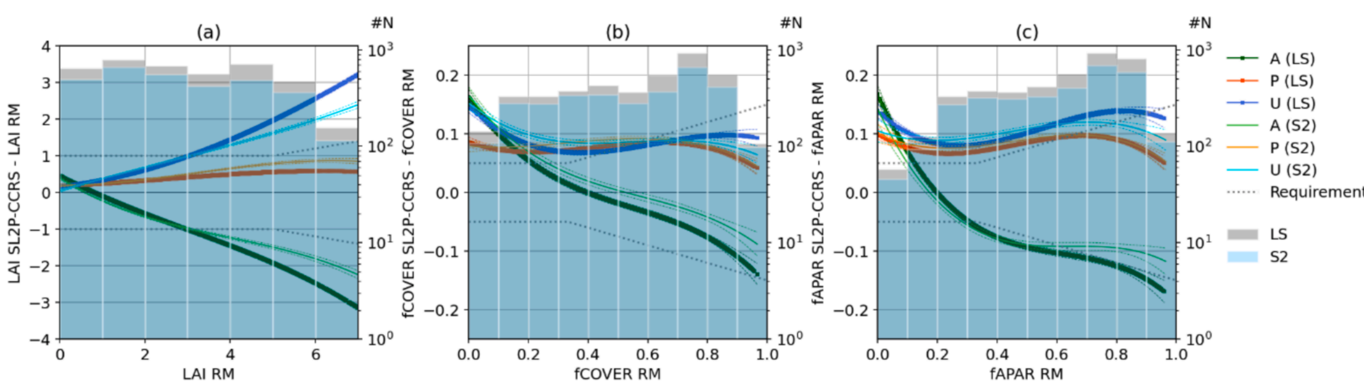

Fig. 5. APU curves and the corresponding 95 % confidence intervals (dashed contours) for SL2P-CCRS estimates of LAI (a), fCOVER (b) and fAPAR (c) obtained from forested classes compared to APU curves for the corresponding estimates from S2. Dashed grey lines bound target user requirements.

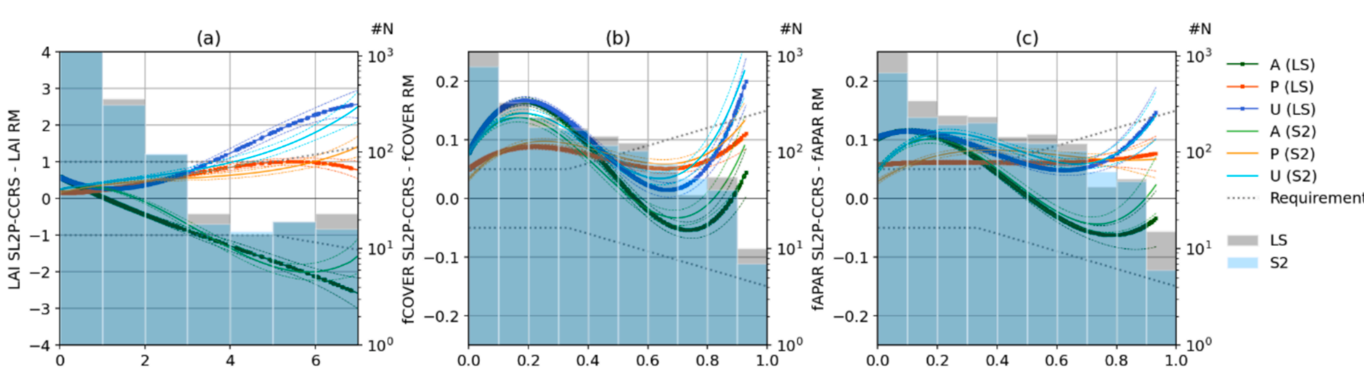

Fig. 6. APU curves and the corresponding 95 % confidence intervals (dashed contours) for SL2P-CCRS estimates of LAI (a), fCOVER (b) and fAPAR (c) obtained from non-forested classes compared to APU curves for the corresponding estimates from S2. Dashed grey lines bound target user requirements.

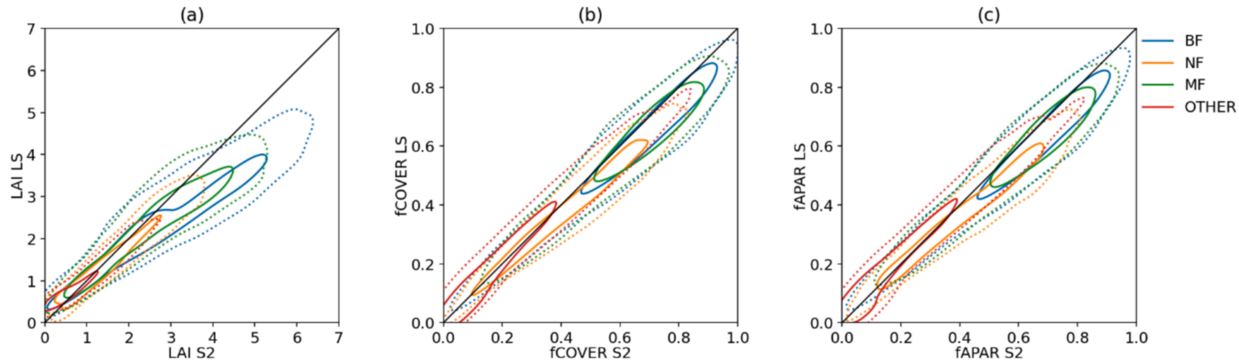

Fig. 7. Density contour plots of SL2P-CCRS LAI (a), fCOVER (b) and fAPAR (c) estimates from LS data compared to the corresponding estimates from S2 data (reference): continuous (dashed) lines present 50 %ile (10 %ile) and continuous black line present the 1:1 line.

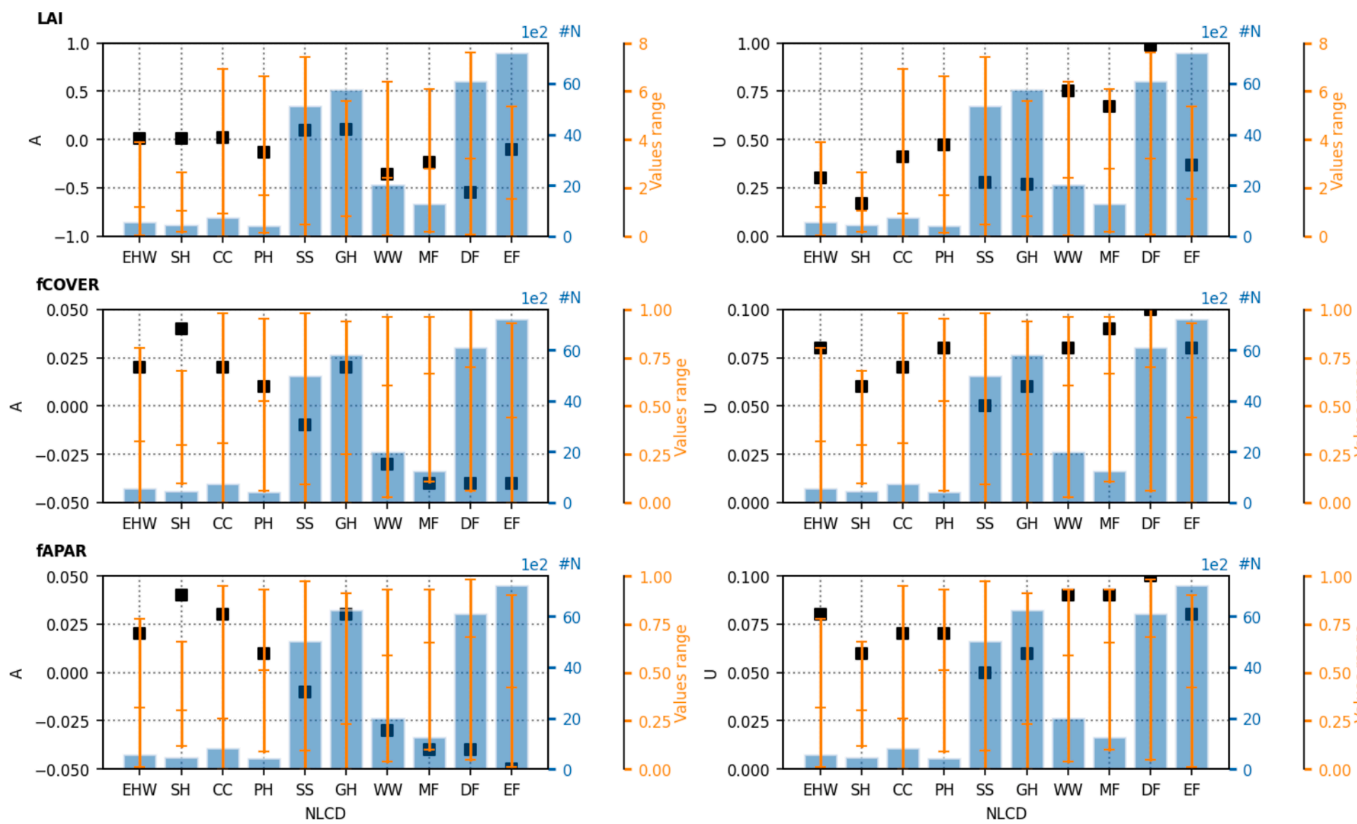

Fig. 8. Class specific A and U statistics between SL2P-CCRS estimates of LAI, fCOVER, and fAPAR from LS and the corresponding estimates from S2 (reference), together with the samples size (histogram) and the variation range of estimates from S2 (bars) as a function of NLCS land cover class.

forested classes, with a positive bias between 0.01 and 0.04 for the former (except for SS) and a negative bias between −0.02 and −0.05 for the latter. These accuracy errors were generally less than 50 % of the corresponding validation A. This was expected since SL2P-CCRS RTMs and RTM priors are identical for S2 and LS. However, U was generally much larger than A, ranging from 0.18 to 1 for LAI and from 0.05 to 0.1 for fCOVER and fAPAR. Even so, intercomparison U for a given cover class was generally less than 75 % of the corresponding validation U for that class (compare Figs. 4 and 8).

3.3. Stability

S was quantified for 46 sites for LS (Fig. 9) and ~30 sites for S2 (Fig. 10). LS S ranged from ~−0.15 yr^{-1} to 0.08 yr^{-1} for LAI with a mean (standard deviation) across sites of −0.01 (0.06) yr^{-1}, and from −0.02 yr^{-1} to 0.02 yr^{-1} for fCOVER and fAPAR with a mean (standard deviation) of 0 (0.01) yr^{-1}. S2 S values ranged between −0.17 yr^{-1} and 0.25 yr^{-1} for LAI with a mean (standard deviation) of 0.02 (0.09) yr^{-1} and from −0.03 yr^{-1} to 0.03 yr^{-1} for fCOVER and fAPAR with a mean (standard deviation) of 0 (0.01) yr^{-1}. LS S confidence intervals ranged from 0.01 to 0.38 for LAI and from 0 to 0.06 for fAPAR and fCOVER. However, confidence intervals for S2 S were ~3 times greater than LS S due to the shorter time span of S2 and RM matchups versus LS and RM matchups.

LS S was weakly correlated with bias (R ~ 0.43 for LAI, ~0.10 for fCOVER, and ~0.06 for fAPAR) and with the site average RMs

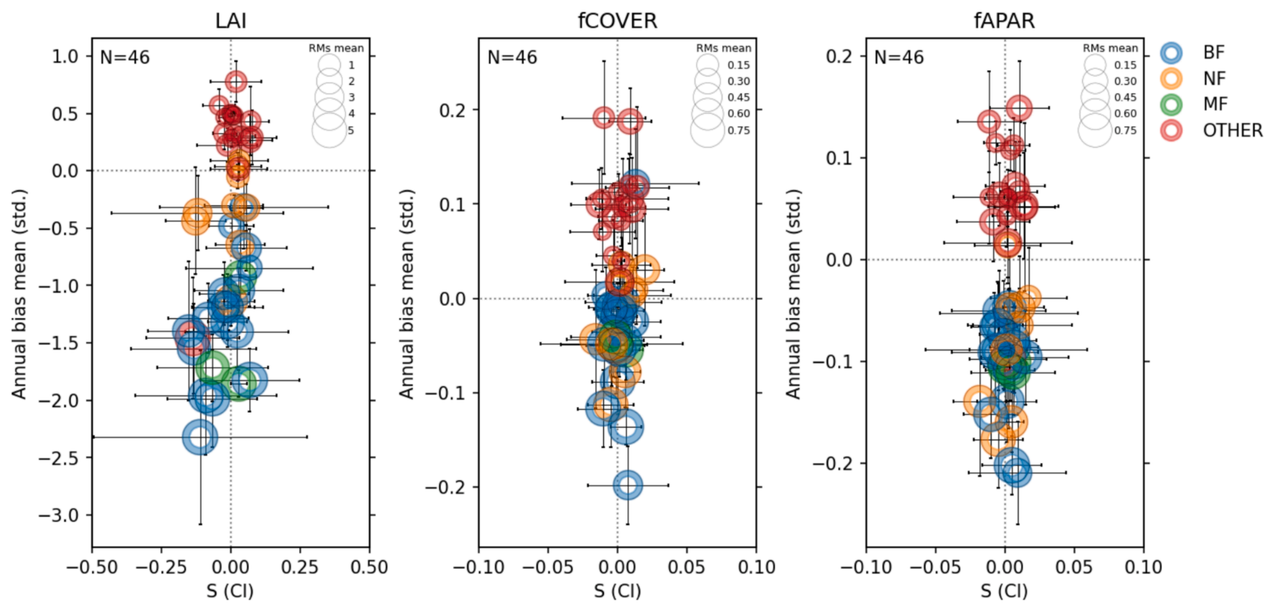

Fig. 9. Scatter plots of LS S versus annual bias mean for SL2P-CCRS estimates of LAI, fCOVER and fAPAR: x error bars (CI: S confidence interval), y error bars (std.: annual bias standard deviation), circles size (RMs mean), and color (groupings of NLCD classes).

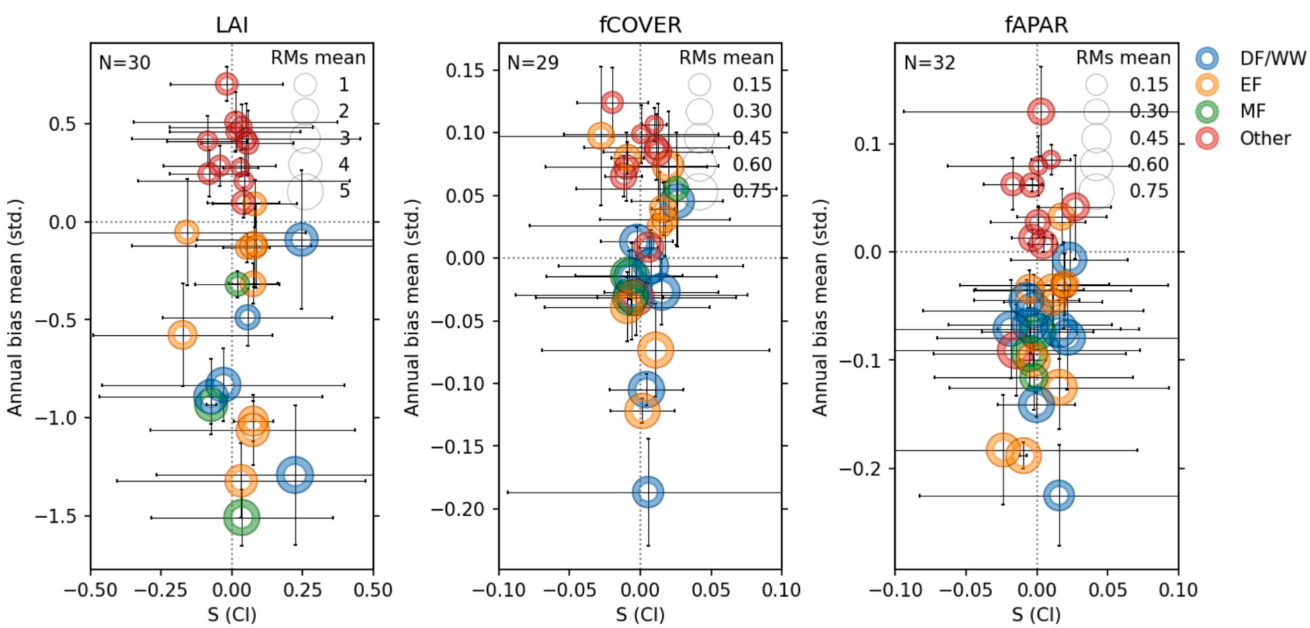

Fig. 10. Scatter plots of S2 S versus annual bias mean for SL2P-CCRS estimates of LAI, fCOVER and fAPAR: x error bars (CI: S confidence interval), y error bars (std.: annual bias standard deviation), circles size (RMs mean), and color (groupings of NLCD classes).

magnitude (R ~ −0.41 for LAI, ~−0.02 for fCOVER, and ~−0.03 for fAPAR). Similarity, S2 S was weakly correlated with bias (R ~ −0.13 for LAI, ~−0.06 for fCOVER, and ~0.18 for fAPAR) and with the site average RMs magnitude (R ~ 0.22 for LAI, ~0 for fCOVER, and ~−0.16 for fAPAR) (Tables F1 and F2 in Appendix F).

4. Discussion

This study focussed on the thematic performance of SL2P-CCRS estimates, derived from four satellite imagers, for three biophysical vegetation variables, fAPAR, fCOVER, and LAI, related to vegetation status and function. These variables are useful both for modelling and monitoring applications but one cannot ignore the fact that spectral vegetation indices are also widely used for monitoring vegetation status and trends (Giovos et al., 2021; Gao et al. 2020; Ferchichi et al., 2022). Our study focused on vegetation biophysical variables, rather than spectral vegetation indices, as they can be easily validated and are thus well suited for quantifying trends and anomalies of vegetation properties.

Our use of RMs from in-situ networks (Brown et al., 2020a; Fernandes et al., 2024a) allowed us to incorporate the uncertainty of estimated residuals when computing validation statistics. These networks are being supplemented by new regional networks that leverage automated measurements and data processing (e.g. Brown et al., 2021a; Brown et al., 2023) but it is critical that they continue long term monitoring. This study extends our previous CEOS Level 3 validation of vegetation variables from S2 to LS and, for the first time for such products, quantifies time-dependent bias in terms of both inter-annual stability and biases that could arise when combining products from different sensors. We directly quantify annual bias by comparisons to RMs. Our approach is in contrast to other studies (Fang et al., 2021; Kang et al., 2021) that approximate stability using inter-annual trends in the theoretical retrieval uncertainty associated with product retrievals, that themselves likely correspond to precision rather than bias and are not traceable to RMs. These other approaches are useful for quantifying drifts in algorithms precision due to changes in sensor characteristics, pre-processing, or land surface conditions but do not reflect GCOS stability requirements or CEOS good practices for quantifying these requirements. Indeed, even our study, while following these good practices reports stability as a % change in bias per year rather than per decade as some of our sites had less than 10 years of annual bias estimates.

Inter-annual stability is a fundamental requirement for use cases such as environmental accounting (Chraibi et al. 2022) and vegetation-climate studies that rely on trend analysis (Xie et al., 2021) and for use cases, such as reclamation assessments, afforestation and reforestation assessment, and disturbance mapping that rely on anomalies (Rochdi et al. 2014; Diniz et al., 2015; Hermosilla et al. 2019; Hird et al., 2021). Quantifying sensor dependent biases is required since currently, only a combination of LS and S2 imagers have the potential for meeting GCOS requirements for ≤10-day products. Moreover, these biases highlight the potential degradation in product performance when using strategies such as harmonizing sensors to the lowest common spectral sampling (e.g. the Harmonized Landsat and Sentinel 2 products, Claverie et al., 2018).

Our study used perhaps the largest RMs dataset for simultaneous fCOVER, fAPAR, and LAI validation to date in terms of spatial and temporal sampling. There are other sources of fAPAR measurements, but these are not yet qualified as RMs and often do not include understory values (Putzenlechner et al., 2019, 2020; Sanchez-Azofeifa et al., 2022). New automated imaging sensors may improve this situation (Brown et al., 2020b). At the same time, our RMs had limitations that impact the representativeness of our results and, to a lesser extent, their statistical confidence. The most significant limitation is that we did not sample sloped terrain or pixels with significant land cover mixtures that products will generally also map, and that users may require information about. Both limitations can be partially addressed from the user perspective by flagging such areas in product metadata using ancillary information. The additional uncertainty due to mixed pixels can also be addressed using high spatial resolution reference maps as performed in Fernandes et al. (2024b) using the original SL2P algorithm. However, validation over sloped terrain requires new RMs that should be a priority for future networks.

We also identified two other limitations with the RMs. The first was the lack of representative woody-to-total area ratio estimates for forested sites not used in our previous work (Fernandes et al., 2023; Fernandes et al., 2024a). Visual assessment of DHPs for four forest sites with canopies > 19 m tall indicated tall and wide trunks with high relative crown base height (Appendix C). These were reprocessed using CANEYE twice to first estimate PAI and then LAI. Since this procedure required manual delineation of green vegetation cover, it was time consuming, requiring over an hour per plot, compared to the automated HemiPy PAI estimation. We used a woody-to-total area ratio uncertainty based on a single study that used HemiPy with green vegetation automatically identified from DHPs with both visible and near-infrared imagery (Brown et al., 2024). This uncertainty of 0.19 is ~twice that of 0.11 from destructive sampling but at the same time is likely less biased than the latter. More work is required to quantify the uncertainty of woody-to-total area ratio using our CANEYE approach specifically and for all approaches in general.

The second limitation was the constant bias observed for retrievals over sites with substantial moss cover. For fCOVER and fAPAR, this bias was due to the RMs not including moss cover. This is a limitation of HemiPy that could be addressed by CANEYE reprocessing. However, in the absence of a good practice for dealing with LAI validation over mosses, we adopted a pragmatic approach of removing the empirical bias by assuming the RM had a constant incorrect offset. This approach underestimates the potential bias and uncertainty of all products at these sites but does not detract from the goal of our study to quantify the consistency and stability of both LS and S2 products since the bias correction is constant. Moreover, this correction did not have a significant impact on either population, or conditional statistics given the fact it was limited to four sites.

Our study used land cover specific algorithms including a Python implementation (Djamai, 2024) of the Simplified Level 2 Prototype Processor (Weiss and Baret, 2020) for S2 and LS over the OTHER class. The SNAP implementation of SL2P was not used as we have identified discrepancies with our implementation that we previously attributed to bugs in the original MATLAB code used to calibrate the SNAP neural networks (Fernandes et al., 2024a). We continue to see studies and applications using the SNAP solution and are concerned that this will both hamper community validation and result in potential errors in downstream use of products derived from SNAP. This can be addressed by open-source publication of the algorithms as is the case for SL2P-CCRS.

The sampling distributions of S2 and LS matchups were imbalanced between land cover classes but were similar between sensors within classes (Fig. 2 versus Fig. 3). This allows for comparison of conditional statistics between sensors without concern for sample dependent differences in metrics. fCOVER and fAPAR from LS and S2 are found unbiased and with virtually identical A ~ 0.03, U ~ 0.13, and UAR ~ 0.60, while LAI was underestimated, with better estimates obtained with S2 (A ~ −0.33, U ~ 0.98, UAR ~ 0.65) compared to LS (A ~ −0.43, U ~ 1.13, and UAR ~ 0.51). For all variables, S2 and LS provided generally similar A, P, and U conditional on RMs although S2 LAI and fCOVER A error is ~ 10 % lower than LS for LAI > 3 and fCOVER > 0.5 (Figs. 6 and 7). Similarity in S2 and LS A and U metrics is also observed on a land cover specific basis, again with S2 showing slightly better A and U for forests (Fig. 4) which could be explained by their predominance for dense canopy samples (Figs. 2 and 3).

Conditional S2 A, P, U curves were virtually identical to those reported in Fernandes et al. (2023) and Fernandes et al. (2024a) using subsets of the RMs with the same algorithms. This suggests that the RMs sample is sufficiently large and diverse so that further sampling has minimal impact conditional metrics. This is important both because it indicates our earlier and current samples are indeed representative of sampled biomes and terrain conditions and that we have achieved a Stage 4 validation that is only limited by the need for continued RMs. For all variables, validation metrics showed far greater sensitivity to land cover than sensor (Fig. 4). Essentially, metrics differed systematically between forested and non-forested classes. For LAI, the non-forested classes were almost unbiased while the forested classes had a negative bias between −0.05 and −2 as also observed in Fernandes et al. (2024). Some of this difference may be due to the limited number of high LAI values for non-forested samples, but the conditional A and U for forest classes were also ~0.5 worse than the non-forest estimate for LAI > 5. Moreover, the systematic difference in biases persisted for fAPAR and fCOVER, although now they were approximately equal in magnitude but opposite in sign. These differences suggest that, unlike LAI, the fAPAR and fCOVER bias is not necessarily due to canopy heterogeneity as hypothesized in Fernandes et al. (2024a) since otherwise we would expect unbiased estimates for non-forests. It may be that RMs are systematically biased since the same pattern was observed for fCOVER and fAPAR. One possibility is that the RMs protocol requires DHP positioned away from canopy elements by at least 2–3 times their width. For forests, this requires DHP points located away from trunks and hence within gaps. The fAPAR and fCOVER biases were small ~0.1 but important since they exceed the current GCOS requirement for U.

Intercomparisons results (Fig. 7) were consistent with the corresponding validation results in terms of similarity for fCOVER and fAPAR retrievals between sensors, and LS showing a greater LAI underestimation than S2. These findings are also consistent with validation results with LS and S2 retrievals agreeing generally within the validation precision, except for LAI over MF, DF, and WW (Fig. 7). For these classes, S2 LAI was substantially higher than LS LAI for LAI > 3 (slope ~0.6). The absence of a similar bias for EF may be due to the relatively low frequency of high LAI values for EF intercomparisons, but a lower underestimation is also obtained for EF LAI validation compared to WW, DF, and MF (Fig. 4). Further, the larger sample size with inter-comparisons confirms that the validation result was not a sampling artifact. It is also unlikely the bias was due to the difference in spatial resolution of the 30 m LS and 20 m S2 input measurements since the bias was largest over dense closed forests where DHP images indicate gaps were generally within crowns rather than large open areas between crowns. Considering the algorithms and matchup methods, the forest bias between S2 and LS supports the hypothesis that it is due to differences in spectral sampling. Indeed, the bias is not likely due to the input SDR processing chain since then it would have been seen with non-forested classes and less dense forests. It has long been noted that signal saturation of visible bands can result in low signal to noise ratios that in turn limit the range of retrieved high LAI values from inversion of RTMs (Myneni et al., 1997). While LS has SWIR bands that may alleviate this problem (Fernandes et al. 2023), SL2P-CCRS assumes identical multiplicative input noise and as such is likely still placing undue weight on the visible bands, specifically the red band of LS. S2, with red-edge bands, may not depend on the low signal to noise ratio for red band as noted by Dong et al. (2023). Indeed, Fernandes et al. (2024b) found the same saturation when using a retrieval algorithm based only on S2 10 m bands that did not include red-edge or SWIR sampling. The systematic bias between S2 and LS could be corrected a posterior using matchups and could be applied to harmonized SDRs.

LS stability fell within GCOS requirements. This was not expected considering the precision error of all products. Indeed, the fCOVER stability of less than 0.02 yr-1 indicates one could detect changes of 0.2 fCOVER per decade, well within the requirement of many systems for tracking reclamation, revegetation, and gradual vegetation cover loss. Granted the stability is based on annual average bias but this is necessary to remove the impact of seasonality or differences in the dates of intra-annual matchups. Comparisons to automated sensor networks can assess seasonal stability but would require a sufficient temporal baseline not widely available currently. S2 stability was similar to LS on average although the range observed was larger due to the shorter S2 period examined. The confidence interval of S2 stability results could be improved by using new Collection 1 data that extends back to 2016.

5. Conclusions

This study evaluated the consistency and stability of SL2P-CCRS estimates of fAPAR, fCOVER and LAI from LS and S2 data over North American forested and non-forested sites. RMs from NEON and regional CCRS sites are used.

Based on 4932 S2-RM comparisons and 6569 LS-RM comparisons, A and U of SL2P-CCRS estimates of fCOVER (A ~ 0.03, U ~ 0.13) and fAPAR (−A ~ 0.03, U ~ 0.13) from LS and S2 are similar. However, LAI estimates from S2 (A ~ −0.33, U ~ 0.98) are slightly better than estimates from LS (A ~ −0.43, U ~ 1.13); with the largest difference observed for LAI > 3 over woody wetlands, deciduous forest, and mixed forest. These results are confirmed by LS against S2 intercomparison showing that SL2P-CCRS estimates from LS and S2 agreed within 0.15 at 50 %ile for fCOVER and fAPAR and within 0.5 at 50 %ile for LAI, except for woody wetland, deciduous forest, and mixed forest, for which substantially lower estimates are generally obtained using LS compared to S2.

The stability of SL2P-CCRS estimates from LS and S2 fell within GCOS requirements with a mean (standard deviation) value over sites of -0.01 yr^{-1} (0.06 yr^{-1}) for LS LAI, 0.02 yr^{-1} (0.09 yr^{-1}) for S2 LAI, and 0 yr^{-1} (0.01 yr^{-1}) for fCOVER and fAPAR from both LS and S2. However, the confidence intervals of S2 stability estimates often exceeded GCOS requirements due to the limited inter-annual overlap with RMs. Nevertheless, the LS stability estimates could be employed to assess observed trends in vegetation both the NEON sites and similar sites in general as envisioned by the Global Climate Observing System concept of essential climate variables of the biosphere.

Our findings support the hypothesis that SL2P-CCRS LAI, fAPAR, and fCOVER products from LS and S2 can be combined to enhance temporal sampling, although sensor specific bias correction should be applied to LAI as recommended in Fernandes et al. 2023. Future studies should exploit these times series to monitor the status and trends of vegetation and to support models of crop productivity, land surface fluxes, and habitat.

CRediT authorship contribution statement

Najib Djamai: Writing – review & editing, Writing – original draft, Visualization, Validation, Software, Methodology, Formal analysis, Conceptualization. **Richard Fernandes:** Writing – review & editing, Supervision, Funding acquisition. **Lixin Sun:** Writing – review & editing. **Gang Hong:** Writing – review & editing. **Luke A. Brown:** Writing – review & editing, Data curation. **Harry Morris:** Writing – review & editing, Data curation. **Jadu Dash:** Writing – review & editing.

Declaration of competing interest

The authors declare that they have no known competing financial interests or personal relationships that could have appeared to influence the work reported in this paper.

Acknowledgement

We acknowledge Dr. Marie Weiss and Dr. Fred Baret for providing the original SL2P code that was used as a basis for the versions of SL2P-CCRS used in this study. We acknowledge the use of modified Sentinel 2 data and derived products. This study has been undertaken using data from GBOV "Ground Based Observation for Validation" (https://land.copernicus.eu/global/gbov) funded by European Commission Joint Research Centre FWC932059, part of the Global Component of the European Union's Copernicus Land Monitoring Service. We thank the National Ecological Observatory Network for the measurements collected in the field under the direction of Dr. Courtney Meier. We thank excellent reviewers and the editors of this paper. The work was funded by Natural Resources Canada's Earth Observation for Cumulative Effects Project.

Appendix A

Table A1
Number of Elementary Sampling Units (ESUs), sampling period, number of acquired samples, and National Land Cover Database (NLCD) classes for CCRS and NEON sites.

Site	Network	Start Date	End Date	#ESUs	NLCD (#samples)
Peace River	CCRS	2019-08-12	2019-08-12	3	DF (3)
YellowKnife	CCRS	2019-08-11	2019-08-12	3	EF (3)
Mer Bleue	CCRS	2019-09-18	2019-09-18	3	EF (2), DF (1)
Hay River	CCRS	2019-09-05	2019-09-07	28	EF (27), MF (1)
Geraldton	CCRS	2020-07-21	2020-07-21	3	EF (2), DF (1)
Nova Scotia	CCRS	2021-08-26	2021-08-27	3	EF (2), DF (1)
Turkey Point	CCRS	2019-06-27	2019-06-27	3	EF (2), DF (1)
Vancouver Island	CCRS	2019-08-09	2019-08-10	3	EF (3)
Mt. Polley	CCRS	2019-08-14	2019-08-15	3	MF (2), EF (1)
Labrador	CCRS	2019-07-24	2019-07-31	12	MF (6), EF (6)
STER	NEON	2014-04-01	2022-09-08	19	CC (357)
KONA	NEON	2017-06-22	2022-10-27	24	CC (221)
TREE	NEON	2015-07-08	2022-06-21	23	DF (145), MF (79), WW (11), EF (3)
UKFS	NEON	2016-04-06	2022-10-25	24	DF (268), EF (55), GH (3)
BART	NEON	2016-04-14	2022-11-17	27	DF (234), MF (128), EF (11)
SERC	NEON	2017-06-16	2022-09-12	25	DF (356), CC (6)
SCBI	NEON	2015-04-29	2022-09-26	27	DF (402), PH (8)
STEI	NEON	2014-05-08	2022-10-18	23	DF (259), MF (3), WW (3)
BLAN	NEON	2015-09-12	2022-06-21	22	DF (126), SS (118), CC (115), PH (10)
CLBJ	NEON	2016-03-23	2022-11-01	25	DF (328), GH (20)
ORNL	NEON	2016-03-09	2022-11-27	31	DF (416), EF (12), PH (9)
LENO	NEON	2014-06-06	2022-09-26	23	DF (193), WW (114)
GRSM	NEON	2017-08-14	2022-10-04	23	DF (319), EF (4)
MLBS	NEON	2016-06-08	2022-12-03	23	DF (214)
BONA	NEON	2014-06-04	2022-10-25	25	DF (93), EF (77), SS (6), MF (3), WW (2)
DELA	NEON	2015-04-19	2022-10-03	26	DF (294), WW (34), EF (4)
HEAL	NEON	2017-07-17	2022-08-22	23	DS (160), SS (15), EF (1)
BARR	NEON	2018-04-26	2022-08-23	23	EHW (64), SH (15)
TEAK	NEON	2013-04-17	2022-08-10	20	EF (91), SS (1)
JERC	NEON	2015-07-28	2022-12-29	26	EF (364), DF (7), MF (4), CC (3)
SOAP	NEON	2018-07-30	2021-09-22	23	EF (150), SS (2)
ABBY	NEON	2016-11-01	2022-11-24	18	EF (139), GH (68), SS (3), MF (1)
YELL	NEON	2018-06-12	2022-11-01	17	EF (72), SS (10), GH (1)
GUAN	NEON	2019-06-13	2022-09-27	24	EF (518)
SJER	NEON	2014-05-16	2022-10-12	23	EF (207), DF (101), GH (30), SS (4)
RMNP	NEON	2016-07-06	2022-09-12	25	EF (82), DF (58), MF (57)
PUUM	NEON	2013-06-11	2022-08-04	23	EF (320)
OSBS	NEON	2017-08-04	2022-10-25	34	EF (435), WW (22), DF (7), MF (6), EHW (4)
WREF	NEON	2018-04-10	2022-11-01	27	EF (176)
DEJU	NEON	2016-08-25	2022-07-05	23	EF (160), SS (8), WW (2)
TALL	NEON	2016-03-16	2022-10-27	23	EF (390), DF (12), MF (9)
KONZ	NEON	2016-05-10	2022-10-17	24	GH (348), DF (4)
NOGP	NEON	2015-07-14	2022-09-19	23	GH (274)
NIWO	NEON	2017-06-19	2022-10-19	24	GH (188), EF (13)
DCFS	NEON	2014-03-26	2022-10-26	23	GH (247)
CPER	NEON	2014-05-08	2022-10-19	23	GH (451)
WOOD	NEON	2014-05-01	2022-10-24	27	GH (361), EHW (11)
HARV	NEON	2014-05-20	2022-07-12	21	MF (244), EF (126), DF (6), WW (2)
UNDE	NEON	2016-04-15	2022-12-29	27	MF (105), WW (100), DF (81)
LAJA	NEON	2013-02-11	2022-09-21	4	PH (455), EF (1)
DSNY	NEON	2017-07-10	2022-08-15	24	PH (452), WW (36)
TOOL	NEON	2021-07-15	2021-07-22	22	SH (111), DS (20), SS (2)
SRER	NEON	2016-04-27	2022-10-24	23	SS (339)
JORN	NEON	2015-06-10	2022-11-01	23	SS (335)
OAES	NEON	2016-03-21	2022-11-15	20	SS (213), GH (110)
ONAQ	NEON	2014-05-22	2022-09-13	23	SS (337), EF (13)
MOAB	NEON	2015-05-13	2022-11-01	23	SS (311), EF (3)

Appendix B

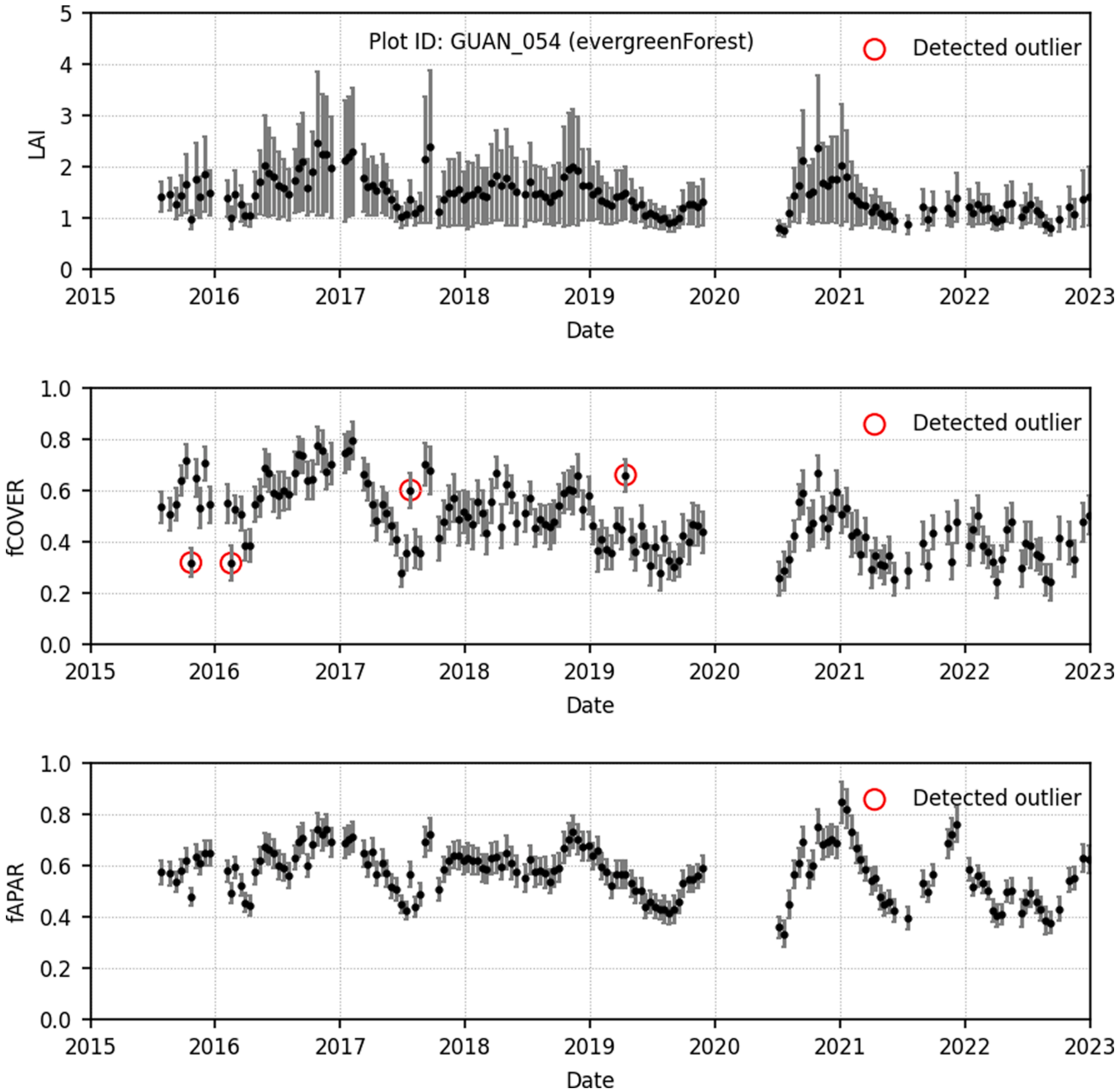

Fig. B1. Example of outliers detected on RMs time series acquired on NEON ESU GUAN_054.

Table B1
Number of samples (N) and number and percentage of outliers detected for each variable and NLCD class for NEON sites.

NLCD	LAI			fCOVER			fAPAR		
	N	#Outliers	% Outliers	N	#Outliers	%	N	#Outliers	% Outliers
EF	3427	3	0.09	3427	30	0.88	3427	16	0.47
GH	2101	1	0.05	2101	4	0.19	2101	3	0.14
SS	1704	0	0	1704	1	0.06	1704	1	0.06
MF	639	1	0.16	639	1	0.16	639	1	0.16
SH	126	0	0	126	0	0	126	0	0
EHW	79	0	0	79	0	0	79	0	0
DF	3923	19	0.48	3923	28	0.71	3923	31	0.79
PH	934	16	1.71	934	55	5.89	934	48	5.14
CC	702	2	0.28	702	16	2.28	702	16	2.28
WW	326	2	0.61	326	2	0.61	326	2	0.61
Total	13,961	44	0.31	13,961	137	0.97	13,961	118	0.83

Appendix C

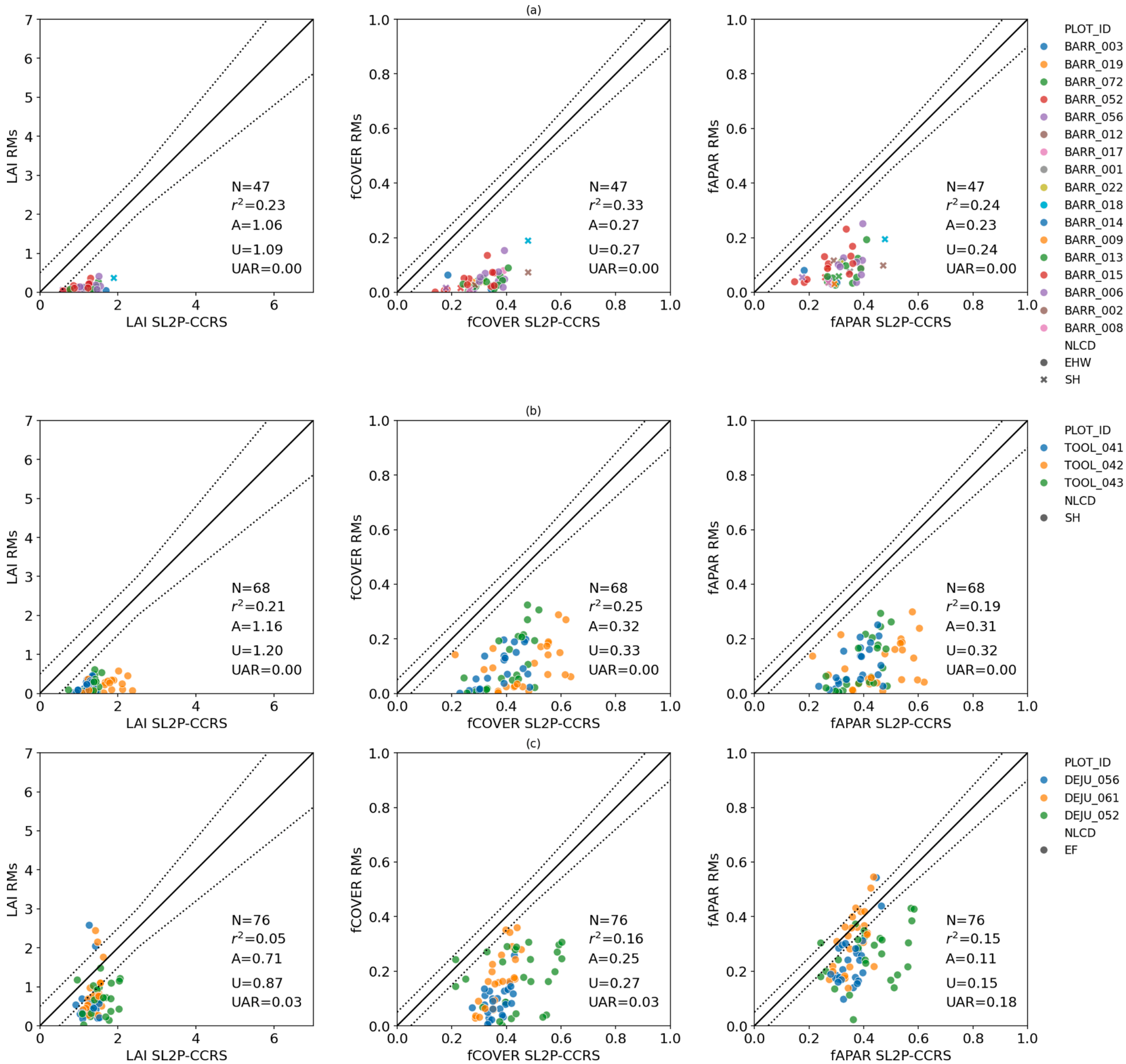

Fig. C1. Scatter plots of SL2P-CCRS estimates of LAI, fCOVER and fAPAR obtained from S2 data versus matching RMs for (a) BARR, (b) TOOL and (c) DEJU sedge sites, together with population validation metrics. Dashed lines bound target user requirement around solid 1:1 line.

Table C1
Woody-to-total area ratios and their uncertainties, in parentheses, applied to RMs. Site corresponds to NEON site ID (Appendix A) or all sites with corresponding SL2P-CCRS land cover classification and overstory canopy height < 19 m.

NLCD (site)	Overstory Woody-to-total area ratio	Understory Woody-to-total area ratios	Source
DF (<19 m)	0.24 (0.11)	0.05	Brown et al., 2021
MF (<19 m)	0.18 (0.11)	0.05	Brown et al., 2021
OTHER (<19 m)	0.10 (0.11)	0.05	Brown et al., 2021
EF (others)	0.16 (0.10)	0.05	Brown et al., 2021
EF (ABBY)	0.70 (0.19)	0.05	This study
EF (WREF)	0.75 (0.19)	0.05	This study
EF (PUUM)	0.65 (0.19)	0.05	This study
EF (TEAK)	0.60 (0.19)	0.05	This study

Appendix D

Table D1
Coefficient of determination (R2), accuracy (A), precision (P) and uncertainty (U) for SL2P-CCRS estimates of LAI, fCOVER and fAPAR from LS data versus matching RMs, as well as the samples size (N) and the variation range (min max) of RMs.

NLCD	LAI						fCOVER						fAPAR					
	N	R^2	A	U	min	max	N	R^2	A	U	min	max	N	R^2	A	U	min	max
EHW	35	0.57	0.12	0.31	0.58	2.07	35	0.65	0.04	0.09	0.12	0.61	35	0.83	0.03	0.07	0.14	0.59
SH	69	0.40	0.01	0.22	0.71	1.88	69	0.56	0.02	0.07	0.24	0.61	69	0.51	0.02	0.07	0.22	0.59
CC	234	0.79	0.30	0.50	0.08	3.95	234	0.82	0.11	0.15	0.00	0.84	234	0.86	0.07	0.11	0.03	0.83
PH	383	0.68	0.39	0.59	0.57	3.81	383	0.69	0.11	0.17	0.04	0.85	383	0.68	0.06	0.13	0.03	0.83
SS	614	0.92	0.26	0.67	0.19	5.88	614	0.90	0.06	0.10	0.00	0.96	614	0.89	0.05	0.10	0.00	0.93
GH	1136	0.72	0.38	0.57	0.10	5.64	1136	0.76	0.11	0.15	0.00	0.93	1136	0.78	0.08	0.13	0.01	0.91
WW	138	0.72	−1.50	1.87	0.58	5.40	138	0.61	−0.09	0.16	0.19	0.89	138	0.46	−0.17	0.22	0.18	0.86
MF	319	0.75	−1.30	1.51	0.52	4.72	319	0.85	−0.05	0.09	0.16	0.89	319	0.73	−0.11	0.15	0.18	0.86
DF	1816	0.74	−1.27	1.68	0.03	5.53	1816	0.76	−0.04	0.12	0.03	0.94	1816	0.73	−0.09	0.15	0.03	0.91
EF	1825	0.67	−0.38	0.82	0.02	4.28	1825	0.71	−0.01	0.12	0.01	0.87	1825	0.67	−0.08	0.14	0.02	0.85
All	6569	0.82	−0.43	1.13	0.02	5.88	6569	0.83	0.02	0.13	0.00	0.96	6569	0.80	−0.03	0.14	0.00	0.93

Table D1
Coefficient of determination (R2), accuracy (A), precision (P) and uncertainty (U) statistics for SL2P-CCRS estimates of LAI, fCOVER and fAPAR from S2 data versus matching RMs, as well as the samples size (N) and the variation range (min max) of RMs.

NLCD	LAI						fCOVER						fAPAR					
	N	R^2	A	U	min	max	N	R^2	A	U	min	max	N	R^2	A	U	min	max
EHW	40	0.49	0.26	0.35	0.12	1.70	40	0.54	0.02	0.06	0.03	0.41	40	0.51	0.02	0.06	0.04	0.41
SH	79	0.24	0.11	0.32	0.59	2.37	79	0.58	0.01	0.07	0.21	0.64	79	0.54	0.01	0.07	0.21	0.62
CC	163	0.77	0.36	0.57	0.01	4.03	163	0.79	0.10	0.15	0.00	0.90	163	0.82	0.07	0.12	0.01	0.88
PH	319	0.63	0.45	0.66	0.15	4.85	319	0.64	0.11	0.17	0.06	0.88	319	0.69	0.06	0.13	0.07	0.86
SS	420	0.86	0.17	0.66	0.00	5.89	420	0.88	0.07	0.11	0.00	0.92	420	0.88	0.05	0.10	0.00	0.90
GH	747	0.75	0.27	0.60	0.00	4.95	747	0.81	0.10	0.14	0.00	0.90	747	0.83	0.05	0.11	0.00	0.85
WW	83	0.63	−1.73	1.99	0.63	5.38	83	0.52	−0.11	0.17	0.20	0.91	83	0.46	−0.17	0.21	0.18	0.89
MF	195	0.84	−1.01	1.21	0.29	5.22	195	0.86	−0.01	0.09	0.03	0.92	195	0.80	−0.09	0.13	0.01	0.89
DF	1330	0.73	−0.87	1.36	0.10	6.87	1330	0.74	−0.02	0.13	0.01	0.99	1330	0.73	−0.08	0.15	0.04	0.95
EF	1556	0.66	−0.39	0.81	0.16	5.00	1556	0.69	0.01	0.12	0.01	0.87	1556	0.67	−0.06	0.13	0.06	0.84
All	4932	0.80	−0.33	0.98	0.00	6.87	4932	0.81	0.03	0.13	0.00	0.99	4932	0.79	−0.03	0.13	0.00	0.95

Appendix E

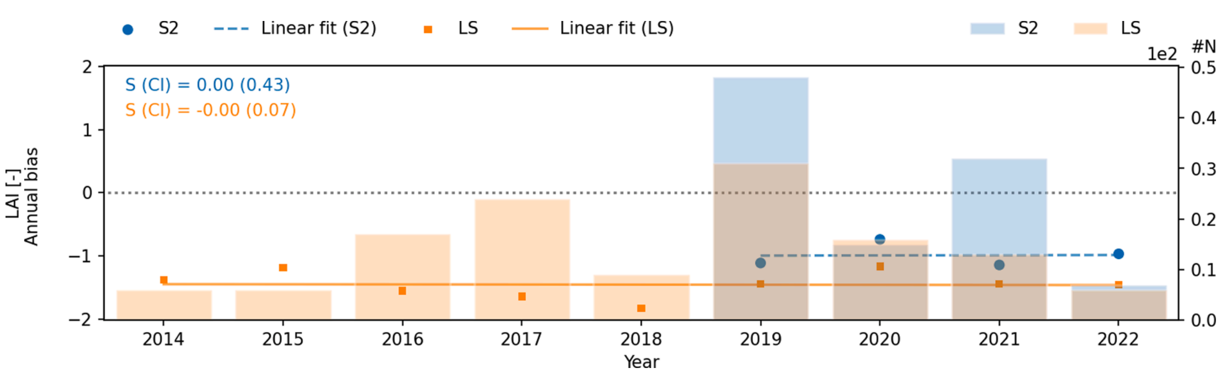

Fig. E1. NEON UNDE site SL2P-CCRS LAI number of annual matchups (N), annual bias time series, ordinary linear regression fits for S2 (blue bars, dots, and dashed line, respectively) and LS (orange bars, dots, and solid line, respectively). The expected value and 95 % confidence interval of S, corresponding to the fitted line slope, are indicated for S2 (blue text) and LS (orange text).

Table E1
Class specific Coefficient of determination (R2), accuracy (A), and uncertainty (U) statistics between SL2P-CCRS estimates from LS data versus the corresponding estimates from S2 data (reference), conjointly with the samples size and the variation range of estimates from S2. N: number samples; min: minimum estimate; max: maximum estimate.

NLCD	LAI						fCOVER						fAPAR					
	N	R2	A	U	min	max	N	R2	A	U	min	max	N	R2	A	U	min	max
EHW	784	0.76	0.03	0.3	0.01	3.9	785	0.74	0.02	0.08	0	0.8	786	0.71	0.02	0.08	0.01	0.78
SH	464	0.8	0.01	0.17	0.17	2.65	464	0.85	0.04	0.06	0.1	0.68	464	0.83	0.04	0.06	0.12	0.66
CC	1169	0.91	0.07	0.38	0	6.92	1078	0.94	0.02	0.07	0	0.98	1312	0.95	0.03	0.07	0	0.95
PH	873	0.89	−0.01	0.37	0.02	6.64	874	0.89	0.01	0.07	0	0.95	876	0.89	0.01	0.07	0.01	0.93
SS	8240	0.92	0.15	0.27	0	7.4	7601	0.95	−0.01	0.04	0	0.98	7649	0.93	0	0.05	0	0.97
GH	8117	0.9	0.14	0.29	0	5.6	8147	0.93	0.02	0.06	0	0.94	8907	0.93	0.03	0.06	0	0.91
WW	3245	0.82	−0.22	0.61	0.02	6.39	3246	0.88	−0.02	0.07	0.03	0.96	3246	0.88	−0.02	0.08	0.02	0.93
MF	2053	0.81	−0.13	0.56	0.17	6.09	2053	0.86	−0.03	0.08	0.1	0.96	2053	0.84	−0.04	0.09	0.1	0.93
DF	10,043	0.87	−0.34	0.8	0.02	7.59	10,050	0.92	−0.03	0.08	0.01	1.01	10,051	0.92	−0.03	0.08	0	0.98
EF	11,805	0.83	−0.1	0.38	0	5.37	11,801	0.86	−0.04	0.08	0	0.93	11,807	0.85	−0.04	0.08	0.01	0.9
All	46,793	0.89	−0.07	0.5	0.02	6.39	46,099	0.93	−0.01	0.07	0.03	0.96	47,151	0.92	−0.01	0.07	0.02	0.93

Appendix F

Table F1
The correlation coefficient R (and the corresponding coefficient interval, CI) between stability (S) for SL2P-CCRS estimates of LAI, fCOVER and fAPAR from LS data and the mean annual bias (mean RMs).

Variable	S vs. Annual bias mean			S vs. RMs mean		
	R	CI (low)	CI (high)	R	CI (low)	CI (high)
LAI	0.43	0.15	0.64	−0.41	−0.63	−0.13
fCOVER	0.10	−0.20	0.38	−0.02	−0.30	0.28
fAPAR	0.06	−0.24	0.34	−0.03	−0.32	0.26

Table F2
The correlation coefficient R (and the corresponding coefficient interval, CI) stability (S) for SL2P-CCRS estimates of LAI, fCOVER and fAPAR from S2 data and the mean annual (mean RMs).

Variable	S vs. Annual bias mean			S vs. RMs mean		
	R	CI (low)	CI (high)	R	CI (low)	CI (high)
LAI	−0.13	−0.47	0.24	0.22	−0.15	0.54
fCOVER	−0.06	−0.42	0.31	0.00	−0.37	0.36
fAPAR	0.18	−0.18	0.50	−0.16	−0.48	0.20

References

Amin, E., Verrelst, J., Rivera-Caicedo, J.P., Pipia, L., Ruiz-Verdú, A., Moreno, J., 2021. Prototyping Sentinel-2 green LAI and brown LAI products for cropland monitoring. Remote Sens. Environ. 255, 112168. https://doi.org/10.1016/j.rse.2020.112168.

Baret, F., Buis, S., 2008. Estimating canopy characteristics from remote sensing observations: review of methods and associated problems. In: Liang, S. (Ed.), Advances in Land Remote Sensing: System, Modeling, Inversion and Application, pp. 173–201. doi: 10.1007/978-1-4020-6450-0_7.

Brown, L.A., Ogutu, B.O., Dash, J., 2019. Estimating Forest Leaf Area Index and Canopy Chlorophyll Content with Sentinel-2: An Evaluation of Two Hybrid Retrieval Algorithms. Remote Sens. (Basel) 11 (15), 1752. https://doi.org/10.3390/rs11151752.

Brown, L.A., Meier, C., Morris, H., Pastor-Guzman, J., Bai, G., Lerebourg, C., Gobron, N., Lanconelli, C., Clerici, M., Dash, J., 2020a. Evaluation of global leaf area index and fraction of absorbed photosynthetically active radiation products over North America using Copernicus Ground Based Observations for Validation data. Remote Sens. Environ. 247, 111935. https://doi.org/10.1016/j.rse.2020.111935.

Brown, L.A., Ogutu, B.O., Dash, J., 2020b. Tracking forest biophysical properties with automated digital repeat photography: A fisheye perspective using digital hemispherical photography from below the canopy. Agric. For. Meteorol. 287, 107944. https://doi.org/10.1016/j.agrformet.2020.107944.

Brown, L.A., Fernandes, R., Djamai, N., Meier, C., Gobron, N., Morris, H., Canisius, F., Bai, G., Lerebourg, C., Lanconelli, C., Clerici, M., Dash, J., 2021a. Validation of baseline and modified Sentinel-2 Level 2 Prototype Processor leaf area index retrievals over the United States. ISPRS J. Photogramm. Remote Sens. 175, 71–87. https://doi.org/10.1016/j.isprsjprs.2021.02.020.

Brown, L., Camacho, F., García-Santos, V., Origo, N., Fuster, B., Morris, H., Pastor Guzman, J., Sanchez-Zapero, J., Morrone, R., Ryder, J., Nightingale, J., Boccia, V., Dash, J., 2021b. Fiducial reference measurements for vegetation bio-geophysical variables: an end-to-end uncertainty evaluation framework. Remote Sens. (Basel) 13 (16), 3194. https://doi.org/10.3390/rs13163194.

Brown, L.A., Morris, H., Leblanc, S., Bai, G., Lanconelli, C., Gobron, N., Meier, C., Dash, J., 2023. HemiPy: a Python module for automated estimation of forest biophysical variables and uncertainties from digital hemispherical photographs. Methods Ecol. Evol. 14 (12), 2329–2340. https://doi.org/10.1111/2041-210X.14199.

Brown, L.A., Morris, H., Morrone, R., Sinclair, M., Williams, O., Hunt, M., Bandopadhyay, S., Guo, X., Akcay, H., Dash, J., 2024. Near-infrared digital hemispherical photography enables correction of plant area index for woody material during leaf-on conditions. Eco. Inform. 79, 102441. https://doi.org/10.1016/j.ecoinf.2023.102441.

Chraibi, E., De Boissieu, F., Barbier, N., Luque, S., Féret, J.B., 2022. Stability in time and consistency between atmospheric corrections: Assessing the reliability of Sentinel-2 products for biodiversity monitoring in tropical forests. Int. J. Appl. Earth Obs. Geoinf. 112, 102884. https://doi.org/10.1016/j.jag.2022.102884.

Claverie, M., Ju, J., Masek, J.G., Dungan, J.L., Vermote, E.F., Roger, J.-C., Skakun, S.V., Justice, C., 2018. The Harmonized Landsat and Sentinel-2 surface reflectance data set. Remote Sens. Environ. 219, 145–161. https://doi.org/10.1016/j.rse.2018.09.002.

Diniz, C.G., de Almeida Souza, A.A., Santos, D.C., Dias, M.C., da Luz, N.C., de Moraes, D.R.V., Maia, J.S., Gomes, A.R., da Silva Narvaes, I., Valeriano, D.M., Maurano, L.E.P., Adami, M., 2015. DETER-B: The new Amazon near real-time deforestation detection system. IEEE J. Sel. Top. Appl. Earth Obs. Remote Sens. 8 (7), 3619–3628. https://doi.org/10.1109/JSTARS.2015.2437075.

Disney, M., Muller, J.-P., Kharbouche, S., Kaminski, T., Voßbeck, M., Lewis, P., Pinty, B., 2016. A new global fAPAR and LAI dataset derived from optimal albedo estimates: Comparison with MODIS products. Remote Sens. (Basel) 8 (275). https://doi.org/10.3390/rs8040275.

Djamai, N., 2024. SL2P-SL2PCCRS_PYTHON. https://github.com/djamainajib/SL2P-SL2PCCRS_PYTHON (Accessed June 2024).

Djamai, N., Fernandes, R., 2018. Comparison of SNAP-derived Sentinel-2A L2A product to ESA product over Europe. Remote Sens. (Basel) 10, 926. https://doi.org/10.1016/j.rse.2019.03.020.

Dong, T., Liu, J., Liu, J., He, L., Wang, R., Qian, B., McNairn, H., Powers, J., Shi, Y., Chen, J.M., Shang, J., 2023. Assessing the consistency of crop leaf area index derived from seasonal Sentinel-2 and Landsat 8 imagery over Manitoba. Canada. Agricultural and Forest Meteorology 109357. https://doi.org/10.1016/j.agrformet.2023.109357.

Doxani, G., Vermote, E., Roger, J.C., Gascon, F., Adriaensen, S., Frantz, D., Hagolle, O., Hollstein, A., Kirches, G., Li, F., Louis, J., Mangin, A., Pahlevan, N., Pflug, B., Vanhellemont, Q., 2018. Atmospheric correction inter-comparison exercise. Remote Sens. (Basel) 10 (2), 352. https://doi.org/10.3390/rs10020352.

Drusch, M., Del Bello, U., Carlier, S., Colin, O., Fernandez, V., Gascon, F., Hoersch, B., Isola, C., Laberinti, P., Martimort, P., Meygret, A., Spoto, F., Sy, O., Marchese, F., Bargellini, P., 2012. Sentinel-2: ESA's optical high-resolution mission for GMES operational services. Remote Sens. Environ. 120, 25–36. https://doi.org/10.1016/j.rse.2011.11.026.

European Space Agency, 2013. Sentinel-2: The operational Copernicus optical high resolution land mission. Retrieved June 23, 2024, from. https://www.esa:int/.

European Space Agency, 2020. Copernicus Sentinel-2 Mission: Calibration and Validation activities. GSICS Quarterly 14 (1). Spring 2020 Issue. Retrieved from dlr.de.

Fang, H., Baret, F., Plummer, S., Schaepman-Strub, G., 2019. An overview of global leaf area index (LAI): Methods, products, validation, and applications. Rev. Geophys. 57 (4), 739–799. https://doi.org/10.1029/2019RG000638.

Fang, H., Wang, Y., Zhang, Y., Li, S., 2021. Long-term variation of global GEOV2 and MODIS leaf area index (LAI) and their uncertainties: An insight into the product stabilities. Journal of Remote Sensing 2021 (9842830). https://doi.org/10.34133/2021/9842830.

Fernandes, R., Baret, F., Brown, L., Canisius, F., Dash, J., Djamai, N., Hong, G., Kalimpalli, S., Latifovic, R., MacDougall, M., Shah, H., Weiss, M., Harvey, K., Sun, L., 2021. LEAF Toolbox: A Software for Environmental and Remote Sensing Data Analysis. https://github.com/rfernand387/LEAF-Toolbox/wiki (Accessed January 2025).

Fernandes, R., Brown, L., Canisius, F., Dash, J., He, L., Hong, G., Huang, L., Le, N.Q., MacDougall, C., Meier, C., Darko, P.O., Shah, H., Spafford, L., Sun, L., 2023. Validation of simplified level 2 prototype processor Sentinel-2 fraction of canopy cover, fraction of absorbed photosynthetically active radiation, and leaf area index products over North American forests. Remote Sens. Environ. 293, 113600. https://doi.org/10.1016/j.rse.2023.113600.

Fernandes, R., Djamai, N., Harvey, K., Hong, G., MacDougall, C., Shah, H., Sun, L., 2024a. Evidence of a bias-variance trade-off when correcting for bias in Sentinel-2 forest LAI retrievals using radiative transfer models. Remote Sens. Environ. 305, 114060. https://doi.org/10.1016/j.rse.2024.114060.

Fernandes, R., Hong, G., Brown, L.A., Dash, J., Harvey, K., Kalimipalli, S., MacDougall, C., Meier, C., Morris, H., Shah, H., Sharma, A., Sun, L., 2024b. Not just a pretty picture: Mapping leaf area index at 10 m resolution using Sentinel-2. Remote Sens. Environ. 311, 114269. https://doi.org/10.1016/j.rse.2024.114269.

Fernandes, R., Plummer, S., Nightingale, J., Baret, F., Camacho, F., Fang, H., Garrigues, S., Gobron, N., Lang, M., Lacaze, R., Leblanc, S., Meroni, M., Martinez, B., Nilson, T., Pinty, B., Pisek, J., Sonnentag, O., Verger, A., Welles, J., Weiss, M., Widlowski, J.L., Schaepman-Strub, G., Roman, M., 2014. Global leaf area index product validation good practices. In: Schaepman-Strub, G., Plummer, S., Nightingale, J. (Eds.), Best Practice for Satellite-Derived Land Product Validation. Land Product Validation Subgroup (Committee on Earth Observation Satellites Working Group on Calibration and Validation). doi: 10.5067/doc/ceoswgcv/lpv/lai.002.

Ferchichi, A., Ben Abbes, A., Barra, V., Farah, I.R., 2022. Forecasting vegetation indices from spatio-temporal remotely sensed data using deep learning-based approaches: A systematic literature review. Eco. Inform. 68, 101552. https://doi.org/10.1016/j.ecoinf.2022.101552.

Ganguly, S., Nemani, R.R., Zhang, G., Hashimoto, H., Milesi, C., Michaelis, A., Wang, W., Votava, P., Samanta, A., Melton, F., Dungan, J.L., Vermote, E., Gao, F., Knyazikhin, Y., Myneni, R., 2012. Generating global leaf area index from Landsat: Algorithm formulation and demonstration. Remote Sens. Environ. 122, 185–202. https://doi.org/10.1016/j.rse.2011.11.017.

Gao, L., Wang, X., Johnson, B.A., Tian, Q., Wang, Y., Verrelst, J., Mu, X., Gu, X., 2020. Remote sensing algorithms for estimation of fractional vegetation cover using pure vegetation index values: A review. ISPRS J. Photogramm. Remote Sens. 159, 364–377. https://doi.org/10.1016/j.isprsjprs.2019.11.018.

Gascon, F., Bouzinac, C., Thepaut, O., Jung, M., Francesconi, B., Louis, J., Lonjou, V., Lafrance, B., Massera, S., Gaudel-Vacaresse, A., Languille, F., Alhammoud, B., Viallefont, F., Pflug, B., Bieniarz, J., Clerc, S., Pessiot, L., Trémas, T., Cadau, E., De Bonis, R., Isola, C., Martimort, P., Fernandez, V., 2017. Copernicus Sentinel-2A calibration and products validation status. Remote Sens. (Basel) 9 (6), 584. https://doi.org/10.3390/rs9060584.

GCOS, 2022. The 2022 GCOS implementation plan. World Meteorological Organization. Retrieved from https://meetings.wmo.int/INFCOM-2/InformationDocuments/INFCOM-2-INF06-1(11-1)-2022-GCOS-IMPLEMENTATION-PLAN_en.pdf (Accessed April 2025).

Giovos, R., Tassopoulos, D., Kalivas, D., Lougkos, N., Priovolou, A., 2021. Remote sensing vegetation indices in viticulture: A critical review. Agriculture 11 (5), 457. https://doi.org/10.3390/agriculture11050457.

Gonsamo, A., Chen, J.M., 2014. Improved LAI algorithm implementation to MODIS data by incorporating background, topography, and foliage clumping information. IEEE Trans. Geosci. Remote Sens. 52 (2), 1076–1088. https://doi.org/10.1109/TGRS.2013.2247405.

Google Earth Engine, 2013. Landsat 8 Level-2 Surface Reflectance (LC08 C02 T1 L2). Accessed June 2024. https://developers.google.com/earth-engine/datasets/catalog/LANDSAT_LC08_C02_T1_L2.

Google Earth Engine, 2021. Landsat 9 Level-2 Surface Reflectance (LC09 C02 T1 L2, https://developers.google.com/earth-engine/datasets/catalog/LANDSAT_LC09_C02_T1_L2 (Accessed June 2021).

Google Earth Engine, 2017. Copernicus Sentinel-2 Surface Reflectance Harmonized. Accessed June 2024. https://developers.google.com/earth-engine/datasets/catalog/COPERNICUS_S2_SR_HARMONIZED.

Group on Earth Observation Global Agricultural Monitoring, 2023. GEOGLAM initiative, stocktaking report 2023-India, https://earthobservations.org/documents/2023/G20_Stocktaking_2023_India.pdf (Accessed June 2024).

Group on Earth Observation Biodiversity Observation Network, 2023. GEOBON strategic plan 2023–2026. https://geobon.org/strategic-plan-new-version-v2 (Accessed June 2024).

Ma, H., Liang, S., 2022. Development of the GLASS 250-m leaf area index product (version 6) from MODIS data using the bidirectional LSTM deep learning model. Remote Sens. Environ. 273, 112985. https://doi.org/10.1016/j.rse.2022.112985.

Hermosilla, T., Wulder, M.A., White, J.C., Coops, N.C., 2019. Prevalence of multiple forest disturbances and impact on vegetation regrowth from interannual Landsat time series (1985–2015). Remote Sens. Environ. 233, 111403. https://doi.org/10.1016/j.rse.2019.111403.

Hird, J.N., Kariyeva, J., McDermid, G.J., 2021. Satellite time series and Google Earth Engine democratize the process of forest-recovery monitoring over large areas. Remote Sens. (Basel) 13 (23), 4745. https://doi.org/10.3390/rs13234745.

Inrae, 2022. CAN-EYE : Software for Canopy Structure Analysis. Accessed June 2024. https://can-eye.paca.hub.inrae.fr.

Kang, Y., Ozdogan, M., Gao, F., Anderson, M.C., White, W.A., Yang, Y., Erickson, T.A., 2021. A data-driven approach to estimate leaf area index for Landsat images over the contiguous US. Remote Sens. Environ. 258, 112383. https://doi.org/10.1016/j.rse.2021.112383.

Knight, E.J., Kvaran, G., 2014. Landsat-8 Operational Land Imager design, characterization and performance. Remote Sens. (Basel) 6 (11), 10286–10305. https://doi.org/10.3390/rs611102860.

Lacaze, R., Smets, B., Baret, F., Weiss, M., Ramon, D., Montersleet, B., Wandrebeck, L., Calvet, J.C., Roujean, J.L., Camacho, F., 2015. Operational 333 m biophysical products of the Copernicus Global Land Service for agriculture monitoring. The International Archives of the Photogrammetry, Remote Sensing and Spatial Information Sciences.

Lang, A.R.G., Yueqin, X., 1986. Estimation of leaf area index from transmission of direct sunlight in discontinuous canopies. Agric. For. Meteorol. 37 (3), 229–243. https://doi.org/10.1016/0168-1923(86)90033-X.

Latifovic, R., Homer, C., Ressl, R., Pouliot, D.A., Hossian, S., Colditz, R., Olthof, I., Chandra, G., Victoria, A., 2012. North American land change monitoring system. In Remote Sensing of Land Use and Land Cover: Principles and Applications 303–324. https://doi.org/10.1201/b11964-24.

Levy, R., Miller, J.A., Barsi, J.A., Thome, K.J., Markham, B.L., 2024. Landsat 9 transfer to orbit of pre-launch absolute calibration of operational land imager (OLI). Remote Sens. (Basel) 16 (8), 1360. https://doi.org/10.3390/rs16081360.

Müller-Wilm, U., 2018. Sen2Cor configuration and user manual, 2nd ed. CS, Toulouse, France.

Myneni, R.B., Ramakrishna, R., Nemani, R., Running, S.W., 1997. Estimation of global leaf area index and absorbed PAR using radiative transfer models. IEEE Trans. Geosci. Remote Sens. 35 (6), 1380–1393. https://doi.org/10.1109/36.649788.

NASA Land Product Validation Subgroup, 2024. Land Product Validation Subgroup Website, https://lpvs.gsfc.nasa.gov/ (Accessed January 2025).

NASA Landsat Science, 2013. Spectral Response of the Operational Land Imager in Band Band Average Relative Spectral Response. Accessed January 2025. https://landsat.gsfc.nasa:gov/satellites/landsat-8/spacecraft-instruments/operational-land-imager/spectral-response-of-the-operational-land-imager-in-band-band-average-relative-spectral-response/.

National Ecological Observatory Network (NEON), 2024. Explore Data Products (Accessed June 2024).

Niinemets, Ü., Tobias, M., 2019. Canopy leaf area index at its higher end: Dissection of structural controls from leaf to canopy scales in bryophytes. New Phytol. 223 (1), 118–133. https://doi.org/10.1111/nph.15767.

Nikon, 2024a. Nikon D810 Overview. https://www.nikonusa.com/p/d810/1542/overview (Accessed June 2024).

Nikon, 2024b. Nikon AF Fisheye Nikkor 16mm f/2.8D Overview. https://en.nikon.ca/p/af-fisheye-nikkor-16mm-f28d/1910/overview (Accessed June 2024).

Nikon, 2024c. Nikon D850 Overview. https://en.nikon.ca/p/d850/1585/overview (Accessed June 2024).

Nikon, 2024d. Nikon AF-S Fisheye Nikkor 8-15mm f/3.5-4.5E ED Overview. https://en.nikon.ca/p/af-s-fisheye-nikkor-8-15mm-f35-45e-ed/20066/overview (Accessed June 2024).

Nikon, 2024e. Nikon ViewNX-i Overview. https://en.nikon.ca/p/viewnx-i/ViewNX_i/overview (Accessed June 2024).

Pipia, L., Amin, E., Belda, S., Salinero-Delgado, M., Verrelst, J., 2021. Green LAI mapping and cloud gap-filling using Gaussian process regression in Google Earth Engine. Remote Sens. (Basel) 13 (3), 403. https://doi.org/10.3390/rs13030403.

Putzenlechner, B., Castro, S., Kiese, R., Ludwig, R., Marzahn, P., Sharp, I., Sanchez-Azofifa, A., 2019. Validation of Sentinel-2 fAPAR products using ground observations across three forest ecosystems. Remote Sens. Environ. 232, 111310. https://doi.org/10.1016/j.rse.2019.111310.

Putzenlechner, B., Marzahn, P., Sanchez-Azofifa, A., 2020. Accuracy assessment on the number of flux terms needed to estimate in situ fAPAR. Int. J. Appl. Earth Obs. Geoinf. 88, 102061. https://doi.org/10.1016/j.jag.2020.102061.

Qiu, S., Zhu, Z., He, B., 2019. Fmask 4.0: Improved cloud and cloud shadow detection in Landsats 4–8 and Sentinel-2 imagery. Remote Sens. Environ. 231, 111205. https://doi.org/10.1016/j.rse.2019.111205.

Rochdi, N., Zhang, J., Staenz, K., Yang, X., David, R., Banting, J., King, C., Doherty, R., 2014. Monitoring procedures for wellsite, in-situ oil sands and coal mine reclamation in Alberta (MOPRA). Oil Sands Research and Information Network, University of Lethbridge,. https://doi.org/10.7939/R3280505Q.

Sanchez-Azofeifa, A., Sharp, I., Green, P.D., Nightingale, J., 2022. Calibration of Co-Located Identical PAR Sensors Using Wireless Sensor Networks and Characterization of the In Situ fPAR Variability in a Tropical Dry Forest. Remote Sens. (Basel) 14 (12), 2752. https://doi.org/10.3390/rs14122752.

Storey, J., Choate, M., Lee, K., 2014. Landsat 8 Operational Land Imager on-orbit geometric calibration and performance. Remote Sens. (Basel) 6 (11), 11127–11152. https://doi.org/10.3390/rs61111127.

Shabanov, N.V., Huang, D., Yang, W., Tan, B., Knyazikhin, Y., Myneni, R.B., Ahl, D.E., Gower, S.T., Huete, A.R., Aragao, L.E.O.C., Shimabukuro, Y.E., 2005. Analysis and optimization of the MODIS leaf area index algorithm retrievals over broadleaf forests. IEEE Trans. Geosci. Remote Sens. 43 (8), 1855–1865. https://doi.org/10.1109/TGRS.2005.852898.

United States Geological Survey, 2019. Landsat 8 data users handbook. Accessed June 2024. https://www.usgs.gov/centers/eros/science/landsat-8-data-users-handbook.

United States Geological Survey, 2022. Landsat 9 data users handbook. Accessed June 2024. https://www.usgs.gov/centers/eros/science/landsat-9-data-users-handbook.

United States Geological Survey (USGS), 2024. National Land Cover Database. Accessed June 2024. https://www.usgs.gov/centers/eros/science/national-land-cover-database.

Verhoef, W., 1985. Earth observation modeling based on layer scattering matrices. Remote Sens. Environ. 17 (2), 165–178. https://doi.org/10.1016/0034-4257(85)90072-0.

Verhoef, W., Bach, H., 2007. Coupled soil–leaf-canopy and atmosphere radiative transfer modeling to simulate hyperspectral multi-angular surface reflectance and TOA radiance data. Remote Sens. Environ. 109 (2), 166–182. https://doi.org/10.1016/j.rse.2006.12.021.

Vermote, E., Roger, J. C., Franch, B., Skakun, S., 2018. LaSRC (Land Surface Reflectance Code): Overview, application and validation using MODIS, VIIRS, LANDSAT and Sentinel 2 data's. In: Proceedings of the IEEE International Geoscience and Remote Sensing Symposium, Vol. 2018, pp. 8173–8176. doi: 10.1109/IGARSS.2018.8517622.

Wan, L., Ryu, Y., Dechant, B., Hwang, Y., Feng, H., Kang, Y., Jeong, S., Lee, J., Choi, C., Bae, J., 2024. Correcting confounding canopy structure, biochemistry and soil background effects improves leaf area index estimates across diverse ecosystems from Sentinel-2 imagery. Remote Sens. Environ. 309, 114224. https://doi.org/10.1016/j.rse.2024.114224.

Weiss, M., Baret, F., 2016. S2ToolBox level 2 products: Version 1.1. https://step.esa.int/docs/extra/ATBD_S2ToolBox_L2B_V1.1.pdf (Accessed June 2024).

Weiss, M., Baret, F., 2020. S2ToolBox level 2 products: Version 2.0. https://step.esa.int/docs/extra/ATBD_S2ToolBox_V2.0.pdf (Accessed June 2024).

WGClimate, 2017. Space agency response to GCOS implementation plan, https://unfccc.int/sites/default/files/962.pdf (Accessed June 2024).

Widlowski, J.L., Taberner, M., Pinty, B., Bruniquel-Pinel, V., Disney, M., et al., 2007. Third Radiation Transfer Model Intercomparison (RAMI) exercise: documenting progress in canopy reflectance models. J. Geophys. Res. 112 (D9), D09111. https://doi.org/10.1029/2006JD007821.

Working Group 1 of the Joint Committee for Guides in Metrology, 2008. Evaluation of Measurement Data—Guide to the Expression of Uncertainty in Measurement. Bureau International des Poids et Mesures, Paris, France.

World Meteorological Organization (WMO), 2022. The 2022 GCOS ECV requirements (GCOS-245), https://library.wmo.int/records/item/58111-the-2022-gcos-ecvs-requirements-gcos (Accessed June 2024).

Xie, X., He, B., Guo, L., Huang, L., Hao, X., Zhang, Y., Liu, X., Tang, X., Wang, S., 2021. Revisiting dry season vegetation dynamics in the Amazon rainforest using different satellite vegetation datasets. Agric. For. Meteorol. 312. https://doi.org/10.1016/j.agrformet.2021.108704.

Yan, K., Park, T., Chen, C., Xu, B., Song, W., Yang, B., Zeng, Y., Liu, Z., Yan, G., Knyazikhin, Y., Myneni, R.B., 2018. Generating global products of LAI and FPAR from SNPP-VIIRS data: theoretical background and implementation. IEEE Trans. Geosci. Remote Sens. 56 (4), 2119–2137. https://doi.org/10.1109/TGRS.2017.2775247.

Yan, K., Park, T., Yan, G., Chen, C., Yang, B., Liu, Z., Nemani, R., Knyazikhin, Y., Myneni, R., 2016. Evaluation of MODIS LAI/FPAR product collection 6. Part 1: Consistency and improvements. Remote Sens. (Basel) 8 (5), 359. https://doi.org/10.3390/rs8050359.

Zotz, G., Kahler, H., 2007. A moss "canopy"–Small-scale differences in microclimate and physiological traits in Tortula ruralis. Flora-Morphol. Distribut. Funct. Ecol. Plants 202 (8), 661–666. https://doi.org/10.1016/j.flora.2007.05.004.

Zupanc, A., 2017. Improving cloud detection with machine learning. Sentinel Hub Blog, https://medium.com/sentinel-hub/improving-cloud-detection-with-machine-learning-2b458d340be1 (Accessed June 2024).